Multiple-scattering theory: new developments and applications

Kumulative Habilitationsschrift

zur Erlangung des akademischen Grades
Dr. rer. nat. habil.

vorgelegt der

Naturwissenschaftliche Fakultät II Chemie und Physik
der Martin-Luther-Universität Halle-Wittenberg

von

Herrn Dr. rer. nat. Arthur Ernst
geb. am 30. November 1968 in Karatau

Contents

Abstract/Kurzfassung

Multiple-scattering theory (MST) is a very efficient technique for calculating the electronic properties of an assembly of atoms. It provides explicitly the Green function, which can be used in many applications such as magnetism, transport and spectroscopy. This work gives an overview on recent developments of multiple-scattering theory. One of the important innovations is the multiple scattering implementation of the self-interaction correction approach, which enables realistic electronic structure calculations of systems with localized electrons. Combined with the coherent potential approximation (CPA), this method can be applied for studying the electronic structure of alloys and as well as pseudo-alloys representing charge and spin disorder. This formalism is extended to finite temperatures which allows to investigate phase transitions and thermal fluctuations in correlated materials. Another novel development is the implementation of the self-consistent non-local CPA approach, which takes into account charge correlations around the CPA average and chemical short range order. This formalism is generalized to the relativistic treatment of magnetically ordered systems. Furthermore, several improvements are implemented to optimize the computational performance and to increase the accuracy of the KKR Green function method. The versatility of the approach is illustrated in numerous applications.

Eine effiziente Methode, die elektronischen Eigenschaften eines Ensembles von Atomen zu berechnen, ist die Vielfachstreutheorie. Sie liefert explizit die Greensche Funktion, die in einer Vielzahl von Anwendungen genutzt werden kann, wie Magnetismus, elektronischer Transport oder Spektroskopie. Diese Arbeit gibt einen Überblick über die jüngsten Entwicklungen im Rahmen der Vielfachstreutheorie. Eine der bedeutensten Neuerungen ist die Implementation von Selbstwechselwirkungskorrekturen im Rahmen des Vielfachstreuformalismus. Diese erlauben erlauben eine realistische Beschreibung der elektronischen Struktur für stark lokalisierte Elektronen. Diese Methode kann in Kombination mit der coherent potential approximation (CPA) ebenso zur Beschreibung von Legierungen und Pseudolegierungen verwendet werden. Dieser Formalismus beinhaltet auch eine Beschreibung für endliche Temperaturen, die die Untersuchung von Phasenübergängen oder thermischen Fluktuationen in korrelierten Systemen gestattet. Eine weitere Neuentwicklung ist die Implementation eines selbskonsistenten Ansatzes für die nicht-lokale CPA, der Ladungswechselwirkungen um das CPA Mittel und chemische kurzreichweitige Ordnung berücksichtigt. Dieser Formalismus ist auf eine relativistische Beschreibung magnetisch geordneter Systeme erweitert worden. Weiterhin wurden zahlreiche Verbesserungen ausgearbeitet, die die numerische Effizienz optimieren und die Genauigkeit der KKR Greens Funktionsmethode erhöhen. Die Vielseitigkeit des Ansatzes wird anhand verschiedener Anwendungen dargestellt.

1. Introduction

Multiple scattering theory is one of the most popular approaches in modern computational solid state physics. It was initiated by Lord Rayleigh in his pioneering work, focused on solving the Laplace equation for the dielectric constant of an inhomogeneous system [1]. Later, the theory of Rayleigh was extended by Kasterin [2] and Ewald [3] who applied it for related problems in optics. In condensed matter physics the multiple-scattering theory was first used for the calculation of stationary electronic states by Korringa [4]. Kohn and Rostoker extended the multiple scattering theory on solving the eigenvalue problem for periodic lattices [5, 6]. Since these publications the theory has come to be known as the Korringa-Kohn-Rostoker (KKR) method for the calculation of electronic structure. After these first publications the KKR method has become very popular among the physicists. The main advantage of the KKR method was a small set of equations and rapid convergence contrary to competing techniques at that time such as the augmented plane wave (APW) approach by Slater [7]. First calculations with the KKR method were done by Ham and Segall [8] who used tabulated structure constants. Later the KKR approach was widely used and further developed for electronic structure calculations, in the 1960's using model crystal potentials and in the seventies in a self-consistent manner within the density functional theory (DFT) in the local spin density (LSD) approximation.

With the advance of the linearized band theory methods by O. K. Andersen [9] the KKR lost its attractiveness because of a complex energy dependency of matrix elements and slow convergency of the structure constants. Although these new methods rely on the multiple-scattering theory, they use the Rayleigh-Ritz variational scheme and are faster in their implementation.

A new impetus in the KKR development was given after reformulation of the multiple scattering theory in terms of the Green function [10–12]. The method became demanded for problems requiring explicitly the Green function. One of such successful applications was the implementation of the coherent potential approximation (CPA) [13] within the multiple-scattering theory [14–16]. This approach is a mean-field theory and designed for studies of substitutionally disordered alloys. Later, it was suggested to use the Green function method also to study the electronic structure of impurities and defects in various host materials [17, 18]. In this approach the Green function of an impurity or an ensemble of atoms embedded in a particular system can be determined in an elegant way by solving a Dyson equation which is associated with the host material via a reference Green function. Thus, already in the seventies the multiple scattering theory became a popular tool for the study of disorder and defects in solids.

Since the KKR method provides explicitly the Green function, this makes it attractive for the calculations of spectroscopic quantities. In the seventies Pendry developed a multiple scattering approach for low energy electron diffraction (LEED), thus providing a powerful tool for the study of solid surfaces [19]. Later, he and co-workers used a similar scheme for a study of the photoemission [20, 21]. Based on a one-step model this method describes the excitation process, the transport of the photoelectron to the surface as well as the escape into the vacuum as a single quantum-mechanical coherent process including all multiple scattering events. This theory was further developed and refined by a number of scientists [22–26]. The formalism of Pendry was later generalized for self-consistent calculations of surfaces and interfaces [27, 28]. The KKR Green function method was as well successfully applied for theoretical description of core-level photoemission[29], Compton scattering [30], X-ray absorption spectroscopies [31, 32], magneto-optics [33, 34], Auger electron spectroscopies [35–37], correlated two-electrons spectroscopies [38, 39]. Approval of the KKR method in spectroscopy was appreciably favored by the development of fully relativistic multiple-scattering theory [40–42].

The multiple-scattering theory was intensively used for development of first-principles approaches for magnetism. Györffy and co-workers developed a mean-field theory of magnetic phase tran-

sitions in metals [43]. Based on this theory the disordered local moment (DLM) approach was developed for electronic structure and magnetic susceptibility of paramagnetic systems [44, 45]. At the same time a multiple-scattering formalism for the dynamical magnetic susceptibility was formulated and applied to paramagnetic and ferromagnetic materials [46]. Later, a multiple-scattering approach for the calculation of exchange parameters in classical Heisenberg model was elaborated by using the force theorem and Lloyd's formula [47]. The first *ab-initio* theory for crystals with non-collinear spin configurations was formulated in terms of a KKR method [48]. Numerous fully-relativistic multiple-scattering implementations were intensively used for calculations of the magneto-crystalline anisotropy of ordered and disordered systems [49–51].

The next step in the evolution of the multiple scattering theory was initiated with the screening transformation introduced by Andersen and Jepsen in the linearized muffin-tin orbital (LMTO) method [52]. In multiple-scattering theory this transformation enables to formulate the KKR problem in terms of a screened reference system with a rapidly decaying Green function [53]. In contrast to the free-particle propagator the reference Green function has a finite spatial extent and can be easily Fourier transformed according to the symmetry of the problem. Due to decoupling of remote lattice sites, semi-infinite systems such as surfaces and interfaces can be treated in an elegant way by using a special iterative technique [54, 55]. The screened KKR matrix becomes tridiagonal or partially sparse. This makes it possible to calculate efficiently electronic structures of large systems with a computational effort of $\mathcal{O}(N)$.

With the advance of all these recent developments and growing computational facilities in the last fifteen years the KKR Green function method became very attractive for first-principle self-consistent studies of a wide range of materials. It was successfully applied in condensed matter physics to conventional systems like bulk, surfaces, interfaces and as well as to exotic materials such as nanowires [56] and clusters with many thousands of atoms [57] . However, later experience with the KKR exposed that most existing self-consistent implementations of the KKR have deffitionces in several aspects.

One of the most serious problems is the angular momentum convergence. The cut-off l_{max} of the angular momentum is the primary convergence parameter of the Green function. As it was pointed out by Butler [58], in principle the multiple-scattering theory is exact in the limit $l_{max} \to \infty$. In practice the KKR calculations have a finite truncation of the angular momentum which is limited by computational resources, which prevents accurate studies of many properties such as the total energy, structural and magnetic phase diagrams, relaxations and surface reconstructions. A slow convergence of the Green function also leads to inaccuracies in the determination of Fermi level, which poses great difficulties in the estimation of the band gap in semiconductors and half-metals. Therefore, a solution for this problem opens new application fields for the multiple-scattering theory.

Another serious problem originates from the LSD approximation which fails to describe systems with localized electrons. This problem is general for any first-principles approach within the LSD approximation, which entails the unphysical interaction of an electron with itself. If some localized electrons are present in the system, like $3d$-electrons in the transition metal oxides, the local density approximation can be essentially improved in this respect by the so-called self-interaction correction (SIC) [59]. In this approach self-interactions of single particle charges, which are present in the LSD approximation, can be removed for the localized electrons. Until now, this approximation was implemented only in variational methods [60, 61]. An implementation of the SIC in the KKR method would be appreciated since it opens new perspectives in numerical first-principles simulations thanks to a straightforward determination of the Green function and a possible generalization to alloys via the CPA. Moreover, the Green function formalism allows to account for static spin fluctuations via the DLM approach and extend the SIC method in a natural way to finite temperatures.

Motivated by the wide-ranging functionality of the multiple scattering theory, we developed a first-principle Green function approach designed for electronic structure calculations of ordered and disordered systems for arbitrary symmetries. We have tried to give account of all experience gained in this field during the past fifty years and extend the method for new applications.

We succeeded to improve essentially numerics of the KKR method, which can provide now total energy calculations with accuracy comparable to well established all-electron variational methods. To apply our method to systems with localized electrons we developed a multiple scattering implementation of the SIC approach and extended it to finite temperatures.

In this thesis I present new aspects of the multiple-scattering theory, which were elaborated during the few years, and demonstrate the efficiency of our method in numerous applications such as magnetism, transport and spectroscopy. The thesis is subdivided in two general parts. The first methodological part includes a brief overview of the KKR method, a discussion about convergence properties of the Green function and the main features of the SIC approach in the multiple scattering formalism. At the end of this part, I introduce the KKR method for layered systems, since surfaces and interfaces were of main interest in my research activity. Some chapters of this part are illustrated by examples, which are not yet published. The second part of the thesis consists of important recent publications, which demonstrate our approach in solving various problems of condensed matter physics.

Most results, presented in this thesis, were obtained with the multiple-scattering program HUT-SEPOT that was developed in a close collaboration of research groups at the Max Planck Institute of microstructure physics (A. Ernst), Daresbury Laboratory (M. Lüders, Z. Szotek, W. M. Temmerman), University of Halle (M. Däne, D. Ködderitsch, G. Fischer, W. Hergert) and University of Bristol (D. A. Rowlands and B. L. Györffy). Some parts of the package were elaborated with essential contributions from J. Henk, L. M. Sandratskii, P. Bruno, I. D. Hughes, J. B. Staunton, P. J. Durham, P. Strange, Y. Wang and G. M. Stocks. This work would have not been possible without helpful consultations with R. Zeller, P. H. Dederichs, H. Ebert, J. Berakdar, B. Yu. Yavorsky, I. Maznichenko, I. Mertig, A. Svane, S. Ostanin, J. Kudrnovský, H. Akai, T. Schulthess, L. Szunyogh, and P. Weinberger.

2. Brief overview of the multiple-scattering theory

The KKR method solves the wave equation using Green functions and, in principle, is quite general. This method has a number of useful features which make it attractive for many applications in the solid state physics. In particular, it separates the purely geometric aspects of the crystal lattice from the dynamics associated with the atoms which constitute the material. Each value of energy and crystal momentum is dealt with directly and independently of any others, with no recourse to a variational principle and no need for orthogonalization. Due to the complex energy integration, the KKR-Green function method is computationally very efficient and is able to solve the geometry problem of an impurity in the bulk or on the clean surfaces without replacing it by an ersatz geometry such as a finite cluster or a supercell. Moreover, the availability of the Green function allows applications to disorder alloys, transport and spectroscopy problems.

2.1. Multiple-scattering theory for ordered systems

Generally, the application of multiple scattering theory for describing electrons in condensed matter systems involves representing each scattering site (atom or ion) as a potential of a finite range. It is convenient to divide the space into distinct sub-volumes so that scattering from a particular scatterer terminates before scattering by another commences. In this case the crystal potential can be written as

$$V(\boldsymbol{r}) = \sum_n V_n(\boldsymbol{r} - \boldsymbol{R}_n) \equiv \sum_n V_n(\boldsymbol{r}_n), \tag{2.1}$$

where $V_n(r)$ is an individual contribution of an atom on site $\boldsymbol{R}_n$. Here $\boldsymbol{r}_n = \boldsymbol{r} - \boldsymbol{R}_n$ denotes the vector between the given vector $\boldsymbol{r}$ from the origin and the vector $\boldsymbol{R}_n$ of the atomic site n (see Figure 2.1). If the potentials of individual scatterers do not overlap and are isotropic, one obtains the so-called *muffin-tin approximation* (MTA). For many systems it is a good approximation to reality and calculations based on it can be fruitful. In the case of a large anisotropy one can use a cell potential expanded in spherical harmonics $Y_L(\boldsymbol{r})$ to fill the space in atomic and interstitial regions:

$$V_n(\boldsymbol{r}_n) = \sum_L V_{nL}(r_n) Y_L(\boldsymbol{r}_n). \tag{2.2}$$

The Kohn-Sham equation can be presented in terms of the Green function:

$$[-\Delta_{\boldsymbol{r}} + V(\boldsymbol{r}) - E] G(\boldsymbol{r}, \boldsymbol{r}'; E) = -\delta(\boldsymbol{r} - \boldsymbol{r}'). \tag{2.3}$$

Most important for electronic structure calculations, the Green function $G(\boldsymbol{r}, \boldsymbol{r}'; E)$ of a perturbed system H is connected to the Green function $G^0(\boldsymbol{r}, \boldsymbol{r}'; E)$ of an unperturbed system H^0 by the Dyson equation (in the operator representation):

$$
\begin{aligned}
G(E) &= G^0(E) + G^0(E) V G(E) = & (2.4) \\
&= G^0(E) + G(E) V G^0(E) = & (2.5) \\
&= G^0(E) + G^0(E) T(E) G^0(E), & (2.6)
\end{aligned}
$$
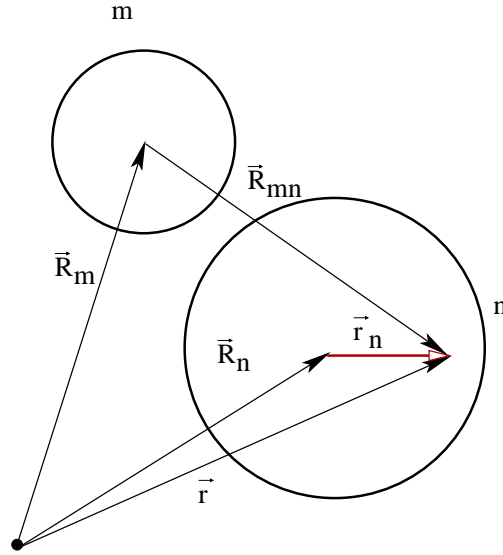
Figure 2.1. Space separation in the multiple scattering expansion

with $V = H - H^0$ the perturbation potential. In the equation (2.6), the scattering matrix T is defined. Iterating equation (2.4) or equation (2.5), one obtains the following implicit equation for T:

$$T(E) = V + VG^0(E)T(E) \qquad (2.7)$$

According to the separation of single-site and crystal quantities in the KKR method, the Green function of the crystal potential is constructed via a Dyson equation starting from the Green function of an isolated potential. In terms of free-particle Green function $G^0(\boldsymbol{r}, \boldsymbol{r}'; E)$ in the real-space representation the Dyson equation for the single-site Green function is given as

$$G_s(\boldsymbol{r}, \boldsymbol{r}'; E) = G^0(\boldsymbol{r}, \boldsymbol{r}'; E) + \int d\boldsymbol{r}'' \int d\boldsymbol{r}''' G^0(\boldsymbol{r}, \boldsymbol{r}''; E)t(\boldsymbol{r}'', \boldsymbol{r}'''; E)G^0(\boldsymbol{r}''', \boldsymbol{r}'; E), \qquad (2.8)$$

where the t-matrix, which is diagonal for a spherical potential, describes the scattering from a single-site potential. The free-particle Green function can be expanded in the angular momentum basis as follows

$$G_0(\boldsymbol{r}, \boldsymbol{r}'; E) = -ip \sum_L j_l(pr_<)h_l^+(pr_>)Y_L(\boldsymbol{r})Y_L^*(\boldsymbol{r}'), \qquad (2.9)$$

where $j_l(z)$ and $h_l(z)$ are respectively spherical Bessel and Hankel functions and $p = \sqrt{E}$. Defining the matrix elements of the single-scattering t-matrix as

$$t_{LL'}^n(E) = \int d\boldsymbol{r}_n \int d\boldsymbol{r}'_n j_l(pr_n)t(\boldsymbol{r}_n, \boldsymbol{r}'_n; E)j_{l'}(pr'_n)Y_L(\boldsymbol{r}_n)Y_L^*(\boldsymbol{r}'_n), \qquad (2.10)$$

one obtains the following expression for the single-scattering Green function:

$$G_s(\boldsymbol{r}_n, \boldsymbol{r}'_n; E) = \sum_{LL'} Z_L^n(\boldsymbol{r}_n; E)t_{LL'}^n(E)Z_{L'}^{n\times}(\boldsymbol{r}'_n; E) - \sum_L Z_L^n(\boldsymbol{r}_<; E)J_L^{n\times}(\boldsymbol{r}_>; E). \qquad (2.11)$$

The building blocks of the Green function are the regular, $Z_L(\boldsymbol{r}; E)$, and irregular, $J_L(\boldsymbol{r}; E)$, solutions of the radial Schrödinger equation at the given (complex) energy E,

$$
\begin{aligned}
Z_L^n(\boldsymbol{r}_n; E) &= \sum_{L'} Z_{LL'}^n(r_n; E) Y_{L'}(\boldsymbol{r}_n), \\
Z_L^{n\times}(\boldsymbol{r}_n; E) &= \sum_{L'} Z_{LL'}^n(r_n; E) Y_{L'}^*(\boldsymbol{r}_n), \\
J_L^n(\boldsymbol{r}_n; E) &= \sum_{L'} J_{LL'}^n(r_n; E) Y_{L'}(\boldsymbol{r}_n).
\end{aligned}
\tag{2.12}
$$

The radial parts of $Z_L^n(\boldsymbol{r}_n; E)$ and $J_L^n(\boldsymbol{r}_n; E)$ functions are matched to spherical Bessel $j_l(z)$ and Hankel $h_l(z)$ functions outside the potential range ($r \geq S$) [62]:

$$
\begin{aligned}
Z_{LL'}^n(r_n; E) &= j_l(pr_n) t_{LL'}^n(E)^{-1} - i p h_l^+(pr_n) \delta_{LL'}, \\
J_{LL'}^n(r_n; E) &= j_l(pr_n) \delta_{LL'}.
\end{aligned}
\tag{2.13}
$$

The t-matrix and corresponding phase shifts can be determined from the normalization conditions of the wave functions [63].

For any assembly of atoms the scattering operator $T(E)$ can be obtained from equations (2.1) and (2.7):

$$
T(E) = \sum_n t^n(E) + \sum_{n \neq m} t^n(E) G^0(E) t^m(E) + \dots
\tag{2.14}
$$

The equation (2.14) separates naturally into partial sums which are characterized by fixed site indices n and m at the leftmost and rightmost single-site t-matrix, respectively. Thus, one can define [12]:

$$
T(E) = \sum_{nm} \tau^{nm},
\tag{2.15}
$$

with $\tau^{nm}(E)$ the scattering path operator which comprises all possible scattering events between the two cells n and m. In real-space multiple scattering theory the Green function for any arrangement of atoms can be expressed in terms of the scattering path operator $\tau^{nm}(E)$:

$$
\begin{aligned}
G(\boldsymbol{r}_n, \boldsymbol{r}'_m; E) &= \sum_{LL'} Z_L^n(\boldsymbol{r}_n; E) \tau_{LL'}^{nm}(E) Z_{L'}^m(\boldsymbol{r}'_n; \varepsilon) \\
&\quad - \sum_L Z_L^n(\boldsymbol{r}_<; E) J_L^m(\boldsymbol{r}_>; E) \delta_{nm}
\end{aligned}
\tag{2.16}
$$

For general electronic systems, the τ-matrix is implicitly given in terms of the t-matrix and the structure constants $g(E)$ representing the free-electron Green function and can be found from the matrix equation:

$$
\tau(E)^{nm} = \left\{ [t(E)^{-1} - g(E)]^{-1} \right\}_{nm}.
\tag{2.17}
$$

The formula (2.17) is the main equation of the KKR Green function method. It yields a complete separation of the potential aspects of a material, expressed in the scattering matrices, from the structural aspects, embodied in the structure constants $g(E)$ of the underling lattice. The structure constants $g(E)$ can be obtained from the equation (2.9) in real space and generalized for any symmetric case by a corresponding Fourier transformation according to symmetry properties of
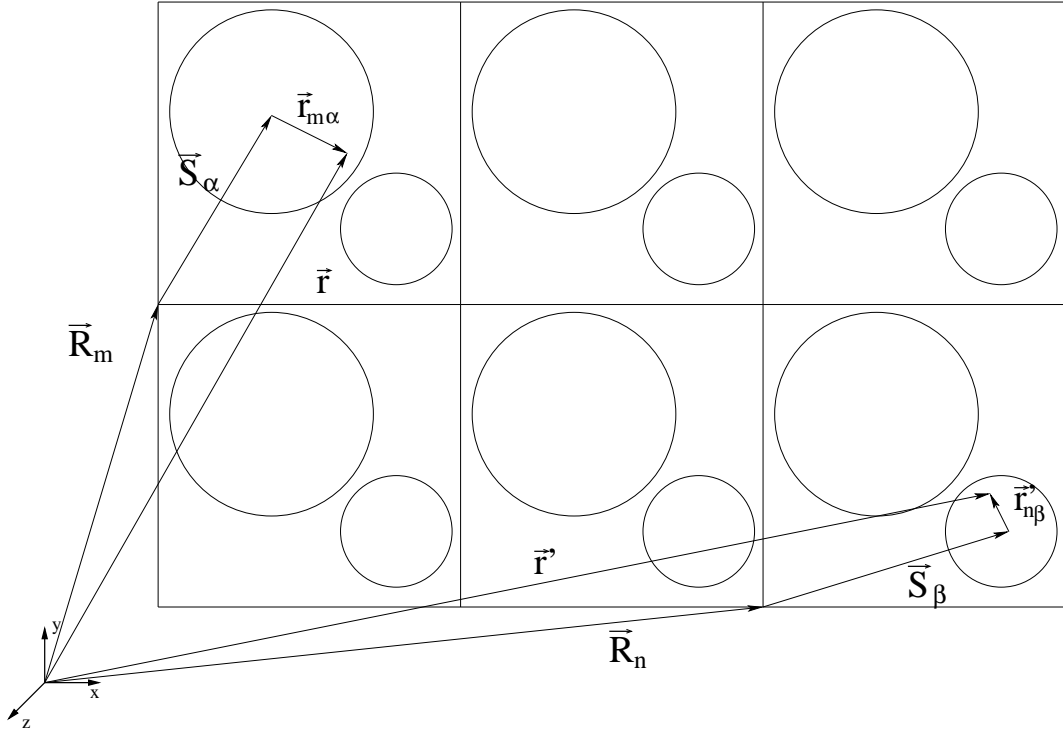
Figure 2.2. Unit cell division of a periodic solid

the problem. In case of 3D periodic solids the lattice Fourier transformation of the structure constants is defined as follows:

$$g_{LL'}^{\alpha\beta}(\boldsymbol{k}, E) \quad = \quad \frac{1}{N} \sum_{mn} g_{LL'}^{m\alpha, n\beta}(\varepsilon) e^{i\boldsymbol{k}\cdot\boldsymbol{R}_{mn}} , \qquad (2.18)$$

where $\boldsymbol{R}_m$ and $\boldsymbol{R}_n$ are direct lattice vectors, α and β denote positions inside the unit cell (Figure 2.2). Then, the scattering path operator in momentum space can be calculated by solving the following Dyson equation:

$$\tau^{\alpha\beta}(\boldsymbol{k}; E) = \left\{ [t^{\alpha}(E)^{-1} - g^{\alpha\beta}(\boldsymbol{k}; E)]^{-1} \right\}_{\alpha\beta} . \qquad (2.19)$$

A similar transformation can be performed in case of two- or one-dimensional periodicities.

Unfortunately, in many cases the direct evaluation of the Fourier transformed structure constants is a highly non-trivial task, mainly due to long-range spatial dependence and slow convergence in real-space. One of the elegant ways to solve this problem is the use of the so-called screening transformation [52, 53]. The main idea is related to the Dyson equation (2.17) which can be easily reformulated with respect to a new reference medium. The free-particle Green function can be replaced by the Green function of the reference system, which can be chosen to have desirable properties such as being more localized spatially then the conventional structure constants. The scattering path operator of a real system can be obtained via the following Dyson equation:

$$\tau = -\Delta m^{-1} + \Delta m^{-1}\left(1 - \Delta m \tau_r\right)^{-1} , \qquad (2.20)$$

where τ_r is the scattering path operator of the reference medium and $\Delta m = t^{-1} - t_r^{-1}$ is the difference of the inverse single-scattering matrices defined by the impurity potential, t and that of the reference medium, t_r. One possible choice for the reference system is a repulsive constant potential medium that is strong enough to raise the bottom of its conduction band above

the energy region of interest [53]. The scattering path operator of this reference systems has a short-range spatial extent and can be easily Fourier transformed. Due to rapid convergence of screened structure constants the KKR matrix becomes sparse or tridiagonal which allows to speed up and efficiently optimize electronic structure calculations of large systems. For semi-infinite layered structures such as surfaces and interfaces the screened KKR matrix has an infinite block-tridiagonal form and can be exactly inverted using special methods such as the principle layer and decimation techniques [55, 64, 65]. This feature is very important for spectroscopy and transport applications because electrons are not artificially confined as in a supercell or a finite slab. In the same manner the screening transformation can be applied as well for nanowires and nanotubes [56]. One possible application of screened KKR method may be to very large systems consisting of hundreds or thousands of different atoms. In this case the matrices that must be inverted are relatively sparse and can be efficiently treated with special numerical techniques [66].

The concept of reference systems can be generalized for any kind of impurities or defects embedded into a host material [17]. Once the Green function of the host is known, the Green function of the system with impurity can be evaluated by the Dyson equation (2.20). Since crystals with impurities may not have any translational symmetry, the Green function of the reference system has to be transformed to the real-space representation. It can be done after solving the KKR problem for the host material in the momentum space. The Green function of the perturbed system (2.20) can be easily evaluated by matrix inversion in real space. In the limit of a single impurity approximation it is quite straightforward to generalize this formalism for random substitutional alloys. In this approach a single impurity is embedded into a periodic self-consistent medium that is averaged over all possible alloy components. This formalism is known as the coherent potential approximation and will be considered in the next chapter.

2.2. Multiple-scattering theory for disordered systems

With regard to ordered, especially, three dimensional periodic systems, the equation (2.17) can be easily solved for the energy E and for the $\boldsymbol{k}$ vector in the first Brillouin zone of the reciprocal lattice. In this case the size of the KKR matrix can be restricted by the size of the unit cell and angular momentum expansion that essentially accelerates the computational speed. The systems with the broken translational symmetry such as clusters, impurities and alloys can be treated by the real-space multiple scattering theory. But solving the KKR equation is limited by the size of the matrix equation (2.17) which can be very large for realistic materials. However, in many random alloys a periodic lattice can be kept, but lattice sites are randomly occupied by atoms of different species. The effective Schrödinger equation for such systems can be solved for a particular configuration which distributes the atoms of the different species over the lattice sites consistent with their concentrations, then it can be statistically averaged over all possible configurations and finally Fourier transformed. Solving this problem is still a difficult task that may be simplified in some mean field approach. The most accurate mean field is the coherent potential approximation (CPA)[13] which in combination with the multiple scattering method provides the first principle KKR-CPA electronic structure computational scheme for random alloys[62, 67].

Virtual crystal approximation. A random substitutional alloy is the simplest type of disorder, which is a material characterized by an underling regular lattice, but all its sites are randomly occupied by either atomic species. The probability of finding a given type of an atom on any lattice site is determined by the relative concentration of that species of atoms within the crystal. This involves an assumption that the site occupancies are uncorrelated, i.e. any short-range correlations or long-range correlations which may exist are neglected. In the case of weak scattering the alloy potential may be assumed to be periodic with the same potential associated with every site and averaged over different atomic types with concentrations c_i and individual potentials V_i:

$$V_C(\boldsymbol{r}) = \sum_i c_i V_i(\boldsymbol{r}) \,. \tag{2.21}$$
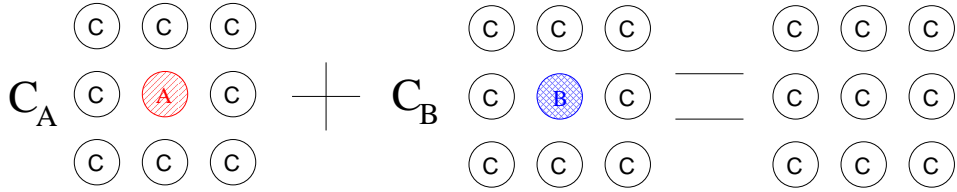
Figure 2.3. Schematic representation of the CPA condition for a binary alloy. The sites labeled "C" are occupied by a coherent potential, while sites labeled "A" and "B" are occupied by impurity potentials.

This assumption constitutes the *virtual crystal approximation* (VCA). The Schrödinger equation for a periodic system with this potential can be solved in standard manner. The virtual crystal approximation is converged at the band edges and it is exact for small perturbations.

Average t-matrix approximation. In systems with localized electronic states the individual atomic potentials become large and the VCA can not correctly describe the electronic structure of the alloy. For small concentrations one can neglect inter-site scattering and permit only the scattering of individual scattering centers. In this so-called *average t-matrix approximation* (ATA) the scattering center is characterized by a single-scattering t-matrix which is averaged over individual single-site scattering t_i-matrices placed on every site of the effective ordered lattice, i.e.

$$t_{ATA}(E) = \sum_i c_i t_i(E). \tag{2.22}$$

For very diluted alloys the ATA can provide relatively accurate results due to the small inter-site correlations at low concentrations. With increasing concentration the inter-site scattering becomes more and more important, and the accuracy of the ATA decreases even further. The average t-matrix approximation is simply a non-self-consistent version of the coherent potential approximation which is generally accepted as the best mean field theory available at the present time for calculating the electronic properties of random substitutional alloys.

Conventional coherent potential approximation. The coherent potential approximation is also built upon scattering theory. In this approximation impurities are embedded into a reference medium which consists of a system with a coherent t-matrix, t_C, on each scattering site. The CPA condition for obtaining the coherent medium is that, on the average, the additional scattering due to replacing a coherent t-matrix by impurity t-matrices, t_i, should vanish (see Fig. 2.3). In terms of the scattering matrix $T(E)$ this condition can be written as

$$T_C(E) = \sum_i c_i T_i(E). \tag{2.23}$$

Here $T_C(E)$ describes scattering from the ordered array of coherent potentials, while $T_i(E)$ describe the scattering from the systems in which the coherent potential is placed on every site except of central one on which, respectively, the individual atom is located. From the equation (2.15) the CPA condition for τ-matrices is given in the following way:

$$\tau_C^{nm}(E) = \sum_i c_i \tau_i^{nm}(E). \tag{2.24}$$

In practice the above condition has to be satisfied only for $n = m = 0$, i.e.

$$\tau_C^{00}(E) = \sum_i c_i \tau_i^{00}(E). \tag{2.25}$$

The scattering path operator of the coherent medium can be evaluated from the following KKR equation (for three-dimensional periodical solids):

$$\tau_C^{00}(E) = \frac{1}{\Omega_{BZ}} \int d\boldsymbol{k} \frac{1}{(t_C^{-1}(E) - g(\boldsymbol{k}; E))} \,. \tag{2.26}$$

Here Ω_{BZ} is the volume of the Brillouin Zone(BZ) and $g(\boldsymbol{k}; E)$ are structure constants in the momentum space representation. As the coherent τ-matrix is known, the impurity τ-matrices τ_i^{00} can be obtained from the Dyson equation

$$\tau_i^{00} = \frac{\tau_C^{00}}{1 + \tau_C^{00}(t_i^{-1} - t_C^{-1})} \,. \tag{2.27}$$

The CPA condition (2.25) is an additional self-consistency condition to the usual charge or potential self-consistency. The following coherent scattering matrix

$$t_C^{new} = \left\{ \frac{\tau_c^{00}(\sum_i c_i \tau_i)^{-1} - 1}{(\sum_i c_i \tau_i)^{-1}} + t_C^{-1} \right\}^{-1} \tag{2.28}$$

provides a working equation to be iterated to solve equations (2.26) and (2.27).

The CPA equations can be easily generalized for any boundary conditions. In contrast to the ATA and other single-site theories, the CPA is exact in both the weak-scattering and the narrow band limits. It has been successfully applied for electronic structure studies of bulk materials, surfaces, interfaces and clusters. However, the CPA remains a single-site approximation and environmental effects on scattering properties are neglected, except on average. This limitation does not allow to investigate fluctuations around the CPA average and to elucidate the influence of atomic short-range order. Such multi-site effects can be systematically taken into account using a *non-local coherent potential approximation* (NLCPA) introduced by Jarrell and Krishnamurthy [68] in the context of a tight-binding model Hamiltonian as the static version of the dynamical cluster approximation. This theory was recently derived within the KKR framework [69–71] [P1,P2].

Nonlocal coherent potential approximation.   In the nonlocal CPA multiple scattering theory one introduces an effective medium represented by the corresponding coherent single-site $\hat{t}$-matrix, the scattering path operator $\hat{\tau}$ and the effective structure constant corrections $\widehat{\delta G}$ to usual KKR structure constants that take into account all multi-site scattering correlations due to the disorder configurations [69–71]. The scattering path operator of this medium describing the average propagation of an electron from site i to site j is given by

$$\hat{\tau}^{ij} = \hat{t}\delta_{ij} + \sum_{k \neq i} \hat{t} \left[G(\boldsymbol{R}_{ij}) + \widehat{\delta G}(\boldsymbol{R}_{ij}) \right] \hat{\tau}^{ij} \,. \tag{2.29}$$

Here a circumflex symbol denotes an effective medium quantity. Since the effective medium is translationally invariant, the scattering path operator can be obtained from the k-space integral representation:

$$\hat{\tau}^{ij} = \frac{1}{\Omega_{BZ}} \int_{\Omega_{BZ}} d\boldsymbol{k} \left[\hat{t}^{-1} - G(\boldsymbol{k}) - \widehat{\delta G}(\boldsymbol{k}) \right]^{-1} e^{i\boldsymbol{k} \cdot (\boldsymbol{R}_i - \boldsymbol{R}_j)} \,. \tag{2.30}$$

Solving this problem is a highly non-trivial task. The main difficulty is to preserve translational invariance and to formulate a consistent treatment in reciprocal space. In the NLCPA this problem is solved by mapping it onto a self-consistently embedded impurity cluster problem, where the
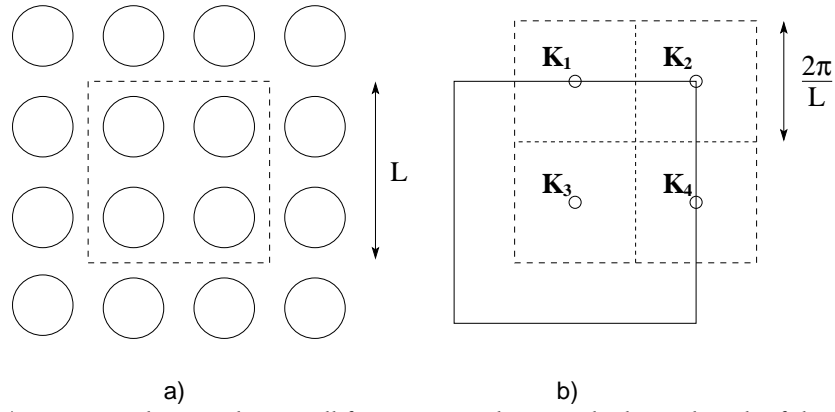
Figure 2.4. *a*) $N_c = 4$ real-space cluster cell for 2D square lattice. The linear length of the tile is $L = 2a$, where a is the lattice constant. *b*) Corresponding reciprocal-space cluster cells. The solid line denotes the 1st BZ. Each tile is centered on a cluster momentum $\boldsymbol{K}$ (dashed line).

configurationally averaged impurity cluster has Born-von Karman boundary conditions imposed. This means that the range of nonlocal scattering correlations included in the medium is restricted by the size of the cluster, but significantly the full translational symmetry of the underlying lattice is retained. This essentially means reducing the size of a conventional lattice to contain only a cluster of N_c sites, so that the edges of the cluster map round to the other end along each axis. Since the lattice constant is unchanged, the boundaries of the BZ will remain the same, however it will now contain only N_c evenly spaced $\boldsymbol{k}$ points referred to as the set of cluster momenta $\{\boldsymbol{K}_n\}$, where $n = 1, .., N_c$. Therefore the conventional lattice Fourier transform used in $N_c \rightarrow \infty$ limit reduces to the cluster Fourier transform

$$\frac{1}{N_c} \sum_{\boldsymbol{K}_n} e^{i\boldsymbol{K}_n \cdot (\boldsymbol{R}_I - \boldsymbol{R}_J)} = \delta_{IJ} \,, \tag{2.31}$$

which relates the real space cluster sites $\{I\}$ to the corresponding set of cluster momenta $\{\boldsymbol{K}_n\}$. The cluster momenta will correspondingly be centered at a set of N_c reciprocal-space tiles which divide up the first Brillouin zone of the lattice. By constructing these coarse graining cells it must be possible to surround the cluster sites with a space-filling tile, the principle axes of which must point along a high symmetry direction of the underling lattice. An example cluster and tile for a square lattice in 2D is shown in Fig. 2.4. In contrast to a supercell approach the size and shape of the real space tiles surrounding the cluster sites corresponds to the size and shape of the reciprocal tiles surrounding the cluster momenta, thus preserving the point-group symmetry of the underlying lattice.

With application of the coarse graining procedure the effective structure constant corrections $\widehat{\delta G}(\boldsymbol{k})$ can be approximated within each of the N_c tiles by the N_c "coarse-grained" values $\widehat{\delta G}(\boldsymbol{K}_n)$, each centered at $\boldsymbol{K}_n$. Then by using Eq. (2.31) one has

$$\begin{aligned}
\widehat{\delta G}(\boldsymbol{R}_{IJ}) &= \frac{1}{N_c} \sum_{\boldsymbol{K}_n} \widehat{\delta G}(\boldsymbol{K}_n) e^{i\boldsymbol{K}_n \cdot (\boldsymbol{R}_I - \boldsymbol{R}_J)} \\
\widehat{\delta G}(\boldsymbol{K}_n) &= \sum_{J \neq I} \widehat{\delta G}(\boldsymbol{R}_{IJ}) e^{-i\boldsymbol{K}_n \cdot (\boldsymbol{R}_I - \boldsymbol{R}_J)}
\end{aligned} \tag{2.32}$$

with I and J denoting the cluster sites at $\boldsymbol{R}_I$ and $\boldsymbol{R}_J$, respectively. The scattering path operator

in reciprocal and real space may be now represented by the set of coarse-grained values

$$\hat{\tau}(\boldsymbol{K}_n) \quad = \quad \frac{N_c}{\Omega_{BZ}} \int_{\Omega_{\boldsymbol{K}_n}} d\boldsymbol{k} \left[\hat{t}^{-1} - G(\boldsymbol{k}) - \widehat{\delta G}(\boldsymbol{K}_n) \right]^{-1} \tag{2.33}$$

$$\hat{\tau}^{IJ} \quad = \quad \frac{1}{\Omega_{BZ}} \sum_{\boldsymbol{K}_n} \left\{ \int_{\Omega_{\boldsymbol{K}_n}} d\boldsymbol{k} \left[\hat{t}^{-1} - G(\boldsymbol{k}) - \widehat{\delta G}(\boldsymbol{K}_n) \right]^{-1} \right\} e^{i\boldsymbol{K}_n \cdot (\boldsymbol{R}_I - \boldsymbol{R}_J)}. \tag{2.34}$$

It is now straightforward to generalize the conventional KKR-CPA in real space and determine the medium by mapping onto an impurity cluster problem. The effective medium scattering path operator may be rearranged in the form

$$\hat{\tau}^{IJ} = \hat{t}_{cl}^{IJ} + \sum_{K,L} \hat{t}_{cl}^{IK} \hat{\Delta}^{KL} \hat{\tau}^{LJ} \tag{2.35}$$

where the effective cluster t-matrix

$$\hat{t}_{cl}^{IJ} = \hat{t}^I \delta_{IJ} + \sum_K t^I \left[G(\boldsymbol{R}_{KL}) + \widehat{\delta G}(\boldsymbol{R}_{IK}) \right] \hat{t}_{cl}^{KJ} \tag{2.36}$$

describes all scattering within the cluster, while the cavity function $\hat{\Delta}_{IJ}$ [72] describes all scattering outside of the cluster. Since $\hat{\Delta}_{IJ}$ describes the medium outside and is independent of the contents of the cluster, it may be used to obtain the impurity cluster path matrix

$$\tau_\gamma^{IJ} = t_{cl,\gamma}^{IJ} + \sum_{K,L} t_{cl,\gamma}^{IK} \hat{\Delta}^{KL} \tau_\gamma^{LJ}, \tag{2.37}$$

where the impurity cluster t-matrix is defined by

$$t_{cl,\gamma}^{IJ} = t_\gamma^I + \sum_K t_\gamma^I G(\boldsymbol{R}_{KL}) t_{cl,\gamma}^{KJ} \tag{2.38}$$

for fixed impurity cluster configuration γ. In other words, the effective cluster has simply been replaced by an "impurity" cluster of real t-matrices with configuration γ and free-space structure constants "embedded" in the effective medium. The KKR-NLCPA self-consistency condition demands that there is no additional scattering from the cluster on the average

$$\hat{\tau}^{IJ} = \sum_\gamma P_\gamma \tau_\gamma^{IJ}. \tag{2.39}$$

Here P_γ is the probability of the configuration γ occurring. The set of numbers $\{P_\gamma\}$ contains the weights for the configurations γ with $\sum_\gamma P_\gamma = 1$. The effective medium t-matrix and structure constant corrections are thus determined from a self-consistent solution of Eq. (2.34) and Eq. (2.39).

The KKR-NLCPA method has relatively low computational cost in comparison with super-cell based methods since the BZ integration does not scale with the cluster size. The accuracy of the method depends only on the number of cluster sites N_c and becomes exact as $N_c \to \infty$.

One of the advantages of the NLCPA is the feasibility to study short-range order effects which is not possible with the conventional CPA method. Short-range order may be included by appropriate weighting the configurations in the equation (2.39) provided the translational invariance is preserved.

More details about the self-consistent NLCPA approach can be found in the publications supplemented in the second part of the thesis.

In the first paper [P1] we present the sell-consistent non-local KKR-CPA method and give a detail description of the implementation. In this work we focus on the methodological aspects of the density functional theory for the NLCPA approach. In particular, the Madelung energy and corresponding charge transfer are discussed in details, supported with calculations of $Cu_{50}Zn_{50}$, $Cu_{60}Pd_{40}$ and $Cu_{77}Ni_{23}$ alloys. We present a way to include short-range order and show how the total energy varies as a function of SRO.

In the next paper [P2] we present a fully relativistic formulation of the KKR-NLCPA method, which is designed for treatment of magnetically-ordered alloys. We elaborate on several improvements for the basic algorithm and a symmetrization of the fundamental coarse-graining procedure, which make it possible to optimize efficiently computational performance of the NLCPA method. The flexibility and power of the resulting implementation is demonstrated by application to the alloy system $Fe_{50}Pt_{50}$.

2.3. Observable quantities and Lloyd formula

Once the scattering path operator is known, the corresponding Green function associated with an individual atomic type can be evaluated from the formula

$$G_{\alpha,\gamma}(\boldsymbol{r}_I, \boldsymbol{r}_J; E) = \sum_{LL'} P_{\alpha,\gamma} Z_L^{\alpha,\gamma}(\boldsymbol{r}_I; E) \tau_{\alpha,\gamma;L,L'}^{IJ}(E) Z_{L'}^{\alpha,\gamma\times}(\boldsymbol{r}_J; E) -$$
$$- \sum_L P_{\alpha,\gamma} Z_L^{\alpha,\gamma}(\boldsymbol{r}_{I<}; E) J_L^{\alpha,\gamma\times}(\boldsymbol{r}_{I>}; E) \delta_{IJ} , \tag{2.40}$$

where $P_{\alpha,\gamma}$ denotes the probability of a cluster configuration with an α-atom at the site I in cluster with configuration γ. The formula (2.40) is general for the KKR-NLCPA, KKR-CPA and KKR for ordered systems because the NLCPA formalism reduces to the conventional CPA at the number of cluster sites $N_c = 1$ and $\gamma = 1$ and, in its turn, the KKR-CPA method amounts to the conventional KKR approach at $\alpha = 1$.

The site-diagonal part of the Green function (2.40) can be used for the calculation of the charge density and the density of states (DOS). The charge density inside the cluster γ of type α located at the site I is given by the expression

$$\rho_{\alpha,\gamma}^I(\boldsymbol{r}_I) = -\frac{1}{\pi} \mathrm{Im} \int_\infty^{E_F} G_{\alpha,\gamma}(\boldsymbol{r}_I, \boldsymbol{r}_I; E) dE , \tag{2.41}$$

whereas the corresponding DOS is given by

$$n_{\alpha,\gamma}^I(E) = -\frac{1}{\pi} \mathrm{Im} \int G_{\alpha,\gamma}(\boldsymbol{r}_I, \boldsymbol{r}_I; E) d\boldsymbol{r}_I , \tag{2.42}$$

where E_F denotes the Fermi energy. The integral over $\boldsymbol{r}_I$ above can be taken over the conventional unit cell at site I, because, through symmetry, the space enclosed by the conventional Wigner-Seitz cells surrounding the cluster sites is equivalent to that enclosed by the tile used for constructing the cluster. In case of the CPA or NLCPA ($\alpha \neq 1$, $\gamma \neq 1$) the total configurationally averaged charge density and DOS per site are simply evaluated by

$$\rho^I(\boldsymbol{r}_I) = \sum_{\alpha,\gamma} P_{\alpha,\gamma} \rho_{\alpha,\gamma}^I(\boldsymbol{r}_I) \tag{2.43}$$

$$n^I(E) = \sum_{\alpha,\gamma} P_{\alpha,\gamma} n_{\alpha,\gamma}^I(E) \tag{2.44}$$

The total average Green function and charge densities are obtained by summing over all γ, and any site in the cluster can be chosen to be site I since all cluster sites are equivalent after averaging over al γ.

The integrated density of states can be evaluated using the Lloyd formula[73, 74], which provides an analytical integration over energy and over all space and directly gives the number of states as a function of energy. Due to its excellent convergence properties the Lloyd formula is very important in the modern multiple scattering theory. Nevertheless the implementation of the Lloyd formula is quite a difficult problem. Analytical properties of terms entering the Lloyd formula hinder its direct implementation. The Lloyd formula entails a logarithmic determinant of the KKR matrix, which is a complex multivalued function of energies and reciprocal vectors. Zeroes of the KKR determinant are complex since the KKR matrix is not Hermitian. One of the serious difficulties is to find the determinant phase throughout the Brillouin zone at the energy at which the number of states is calculated. Despite of these problems the Lloyd formula was successfully implemented in many multiple-scattering codes [30, 75–81]. However, in most implementations the Lloyd formula was used for impurity problems to calculate Friedel charge density oscillations. The convergence properties of the Lloyd integrated density of states were not demanded. Significant progress has been achieved after the extension of the Lloyd formula to complex energies[30, 75–77], which allows to apply it in many applications requiring integration over a complex energy contour. Nevertheless, due to numerical problems with the complex multivalued logarithm of the KKR determinant, the Lloyd integrated density of states was rarely used as a constituent of self-consistent calculations.

However, we have found an elegant way to solve these problems and to incorporate the Lloyd formula in self-consistent calculations. The terms entering the Lloyd formula can be regrouped in a special manner, so that the most time-consuming $\boldsymbol{k}$-dependent part, the KKR matrix, is transformed into a new form, which is a complex single-valued function for all $\boldsymbol{k}$ vectors and can be directly evaluated at a particular energy. Only one single-site term, namely the logarithmic determinant of the Jost function, remains to be multivalued, whose phase can be easily corrected using analytical properties of a complex logarithmic function. Here I give an expression of the Lloyd formula for the complex generalized integrated density of states as it is implemented in the HUT-SEPOT code, which is general for ordered ($\alpha = 1$, $\gamma = 1$, $\widehat{\delta G}(\boldsymbol{K}_n; E) = 0$) and disordered ($\alpha \neq 1$, $\gamma \neq 1$) systems:

$$
\begin{aligned}
\bar{Z}(E) = Z_0(E) &- \frac{1}{\pi\Omega_{BZ}} \left\{ \sum_{\boldsymbol{K}_n} \int_{\Omega_{\boldsymbol{K}_n}} d\boldsymbol{k} \ln \left\| 1 - \widehat{t}(E) \left[\widehat{\delta G}(\boldsymbol{K}_n; E) + G(\boldsymbol{k}; E) \right] \right\| \right\} - \\
&- \frac{1}{\pi N_c} \sum_{\alpha,\gamma} P_{\alpha,\gamma} \ln \left\| 1 - \left[t_{\alpha,\gamma}(E) - \widehat{t}(E) \right] \widehat{\tau}(E) \right\| + \frac{1}{\pi N_c} \sum_{\alpha,\gamma} P_{\alpha,\gamma} \ln \left\| \chi_{\alpha\gamma}(E) \right\| ,
\end{aligned}
\tag{2.45}
$$

where $Z_0(E)$ is a generalized complex integrated density of states of a reference system (free particles or a reference medium) and $\chi(E)$ is the Jost function obtained from the regular solution of the Schrödinger equation. The equation (2.45) enables direct calculations of the integrated density of states

$$
N(E) = \mathrm{Im}\bar{Z}(E) \tag{2.46}
$$

at a single energy in the complex plane without knowledge of the logarithmic function phases at other energy points. Since the Lloyd formula has extraordinary convergence properties in the angular momentum summation and spatial integration, the equation (2.45) can be used for accurate estimation of the valence band energy and correction of the charge density (2.41) and density of states (2.42) that can be performed at each energy. It is quite essential for applications such as structural and magnetic phase transitions, phase stability properties and relaxations. The convergence properties of the Green function and Lloyd corrections will be discussed in Sec. 3.1.

2.4. **Multifunctional KKR Green function code HUTSEPOT**

Most of the results presented in this thesis have been obtained with the multifunctional code HUTSEPOT based on the multiple scattering theory and designed for electronic structure calculations of ordered and disordered systems such as bulk materials, surfaces, interfaces and atomic clusters embedded in different hosts. The development of the code was started in Daresbury Laboratory (A. Ernst, Z. Szotek, W. M. Temmerman and P. J. Durham). Initially it was designed for non-self-consistent calculations of photoemission spectra using a real-space Green function approach [82]. Later the code was extended to two-dimensional systems and made self-consistent. With help of L. Szunyogh and P. Weinberger we implemented the screening transformation and decimation technique which enables correct numerical treatment of semi-infinite systems such as surfaces and interfaces [65]. The real-space photoemission program was adopted for 2D geometry and made use of self-consistent potentials [26].

Since 1999 the HUTSEPOT code has been developed mainly in three institutions: Max Planck Institute of microstructure physics (Halle), Daresbury Laboratory (U. K.) and University of Halle in active cooperation with the University of Bristol and the University of Warwick. It has been generalized to bulk materials, surfaces, interfaces and real-space clusters (A. Ernst, M. Lüders, M. Däne, D. Ködderitsch). For treatment of disorder, the CPA has been implemented in all code modules. Later on the HUTSEPOT has also been extended to allow the first self-consistent non-local CPA calculations (D. A. Rowlands, A. Ernst, J. B. Staunton, B. L. Györffy) [P1].

The code makes use of various potential shape constructions. We implemented the muffin-tin (MT) concept, atomic sphere approximation (ASA) and Voronoi polyhedra for unit cell division. The potentials and charge densities can be represented in both spherical and non-spherical approximations. The full-potential approach together with implemented Lloyd formula improves convergence properties of the Green function essentially and enables electronic structure calculations with an accuracy comparable to other well established methods. Moreover, full convergence of the Green function with relative small angular momentum truncation makes it possible to study semiconducting and insulating materials.

The HUTSEPOT is the first multiple scattering theory based code, specially designed for electronic structure studies of systems with localized electrons. These systems cannot be correctly described within the LSD approximation since it contains an unphysical interaction of electrons with themselves, which is quite considerable for localized electrons. This interaction can be removed with the *self-interaction correction* (SIC) [59]. We implemented a simplified version of the SIC [P5] using the single-site approximation for strongly localized electrons. This opens new application fields for multiple scattering theory, for instance, transition metal oxides, rare-earth and actinide compounds.

With the aim of studying the electronic transport we implemented an approach to compute conductances of tunnel junctions within the framework of the Landauer-Büttiker theory [83]. Combined with a self-consistent Green function method this approach is intensively used for calculations of tunnel junctions in realistic systems [P7,P8]. This part of the HUTSEPOT code will be extended for computing conductances in real-space to describe transport processes in scanning tunnelling microscopy (this work is now in progress).

Recently we have implemented the calculation of exchange interaction parameters and adiabatic spin waves using magnetic force theorem [47] in the multiple-scattering formalism (A. Ernst, G. Fischer, M. Däne, W. Hergert and L. M. Sandratskii). The critical temperature of magnetic transitions can be evaluated both in the mean-field and random-phase approximations. We have used this part of the HUTSEPOT code to study magnetic properties of transition metal oxides and diluted magnetic semiconductors. At the moment we are developing a non-adiabatic spin dynamic approach using the frequency-dependent magnetic susceptibility (P. Buczek, L. M. Sandratskii, A. Ernst and P. Bruno).

The HUTSEPOT is efficiently parallelized using various numerical algorithms. Different loops are optimized using MPI, OPENMP and combined MPI+OPENMP libraries. Especially effective is a

hybrid MPI+OPENMP method when different parallelization schemes are used to span enclosed loops, for instance, for the energy and k integrations. Applying a special MPI groups technique the processors can be separated into different groups, each of them can be used for solving a particular problem. This enables efficient calculations of various structures with many hundreds of atoms. For large systems the HUTSEPOT achieves near linear scaling with 1000 processors on IBM SP5 computers.

3. Total energy and convergence properties of the KKR method

The aim of most first-principles methods is to perform accurate total energy calculations. In principle, density functional theory can provide the exact total energy if the corresponding exchange-correlation energy is known. For real systems the exchange-correlation energy is difficult to determine and it is usually approximated by some known functionals obtained for some more simpler systems. One of the most popular approaches is the local spin density approximation, in which the exchange-correlation energy of an inhomogeneous system is approximated by the exchange-correlation energy of a homogeneous but interacting electron gas, which can be evaluated accurately, e.g., by using Quantum Monte Carlo techniques. In many cases the LSDA works well and has already been widely used for three decades for a great variety of systems. However, the accuracy of total energy calculations does not depend only on the approximation for the exchange-correlation energy. The crucial point is the choice of an appropriate method for solving DFT equations. The multiple-scattering theory can in principle provide a very accurate solution of the DFT equations if the Green function converges well with respect to the number of angular momentum states. As it was already pointed out in the literature [58, 84, 85], the total energy, provided with standard KKR implementations, converges very slowly with this number, which hinders the use of the multiple scattering theory for many applications requiring accurate total energy calculations. Here there is presented a scheme of the total energy calculation in the HUTSEPOT code. The approach is discussed to accelerate the convergence of the Green function.

3.1. Total energy

Since the self-consistent charge density (2.42) is known, the total energy can be calculated. Here the total energy expression is given as it is implemented in the HUTSEPOT code for the NLCPA approach [86] (the conventional CPA is a particular case of this with $\gamma = 1$, $\alpha \neq 1$ and it reduces for ordered systems with $\gamma = 1$, $\alpha = 1$):

$$
\begin{aligned}
E[\rho] =& E_F N(E_F) - \int_{-\infty}^{E_F} dE \, N(E) - \frac{1}{N_c} \sum_{\alpha,\gamma} P_{\alpha,\gamma} \sum_I \int d\boldsymbol{r}_I \rho_{\alpha,\gamma}(\boldsymbol{r}_I) V_{\alpha,\gamma}(\boldsymbol{r}_I) + \\
&+ \frac{1}{2} \frac{1}{N_c} \sum_{\alpha,\gamma} P_{\alpha,\gamma} \sum_{I,J} \left[\int d\boldsymbol{r}_I \int d\boldsymbol{r'}_J \frac{\rho_{\alpha,\gamma}(\boldsymbol{r}_I)\rho_{\alpha,\gamma}(\boldsymbol{r'}_J)}{|\boldsymbol{r}_I - \boldsymbol{r'}_J - \boldsymbol{R}_{IJ}|} - 2 \int d\boldsymbol{r}_I \frac{\rho_{\alpha,\gamma}(\boldsymbol{r}_I) Z_{\alpha,\gamma}^J}{|\boldsymbol{r}_I - \boldsymbol{R}_J|} \right] + \\
&+ \frac{1}{2} \frac{1}{N_c} \sum_{\alpha,\gamma} P_{\alpha,\gamma} \sum_{I,J \neq I} \frac{Z_{\alpha,\gamma}^I Z_{\alpha,\gamma}^J}{\boldsymbol{R}_{IJ}} + \\
&+ \frac{1}{2} \frac{1}{N_c} \sum_{\alpha,\gamma} P_{\alpha,\gamma} \sum_I \sum_{n \notin C} \left[\int d\boldsymbol{r}_I \int d\boldsymbol{r'}_n \frac{\rho_{\alpha,\gamma}(\boldsymbol{r}_I)\bar{\rho}(\boldsymbol{r'}_n)}{|\boldsymbol{r}_I - \boldsymbol{r'}_n - \boldsymbol{R}_{In}|} - 2 \int d\boldsymbol{r}_I \frac{\rho_{\alpha,\gamma}(\boldsymbol{r}_I)\bar{Z}^n}{|\boldsymbol{r}_I - \boldsymbol{R}_{In}|} \right] + \\
&+ \frac{1}{2} \frac{1}{N_c} \sum_{\alpha,\gamma} P_{\alpha,\gamma} \sum_I \sum_{n \notin C} \frac{Z_{\alpha,\gamma}^I \bar{Z}^n}{\boldsymbol{R}_{In}} + \\
&+ \frac{1}{N_c} \sum_{\alpha,\gamma} P_{\alpha,\gamma} \sum_I \int d\boldsymbol{r}_I \rho_{\alpha,\gamma}(\boldsymbol{r}_I) V_{\alpha,\gamma}^{xc}[\rho_{\alpha,\gamma}(\boldsymbol{r}_I)],
\end{aligned}
\tag{3.1}
$$

where $N(E)$ is the integrated density of states, $\rho_{\alpha,\gamma}(\boldsymbol{r}_I)$ is the charge density, $V_{\alpha,\gamma}(\boldsymbol{r}_I)$ is the effective crystal potential of type α inside the cluster γ located at the site I, and $V_{\alpha,\gamma}^{xc}[\rho_{\alpha,\gamma}(\boldsymbol{r}_I)]$ is the corresponding exchange-correlation potential. The average density and nuclear charges

placed on all sites outside the clusters are given by

$$\bar{\rho}(\boldsymbol{r}_n) \quad = \quad \frac{1}{N_c} \sum_I \sum_{\alpha,\gamma} P_{\alpha,\gamma} \rho_{\alpha,\gamma}(\boldsymbol{r}_I) \,, \tag{3.2}$$

$$\bar{Z}^n \quad = \quad \frac{1}{N_c} \sum_I \sum_{\alpha,\gamma} P_{\alpha,\gamma} Z_{\alpha,\gamma}^I \,. \tag{3.3}$$

The first three terms in the equation (3.1) represent the configurationally averaged kinetic single particle energy. It can be seen that the fourth, the fifth and the sixth terms involve the Coulomb interaction between all cluster sites for each fixed impurity configuration γ resulting from the fact that there will be a net (and different) overall charge on each cluster site. After the average over all configurations γ is taken, charge neutrality will be restored. The off-diagonal part of the equation (3.1) above (i.e., when $I \neq J$) arises from charge correlations between the cluster sites, such terms being absent in the conventional single-site KKR-CPA expression. The Madelung energy contribution to the total internal energy per site, which is missing in the single site KKR-CPA, may therefore be calculated as

$$E_M = \frac{1}{2} \frac{1}{N_c} \sum_{\alpha,\gamma} P_{\alpha,\gamma} \sum_{I,J \neq I} \int \int d\boldsymbol{r}_I d\boldsymbol{r}'_J \left[\frac{\{\rho_{\alpha,\gamma}(\boldsymbol{r}_I) - Z_{\alpha,\gamma}^I \delta(\boldsymbol{r}_I)\}\{\rho_{\alpha,\gamma}(\boldsymbol{r}'_J) - Z_{\alpha,\gamma}^J \delta(\boldsymbol{r}'_J)\}}{|\boldsymbol{r}_I - \boldsymbol{r}'_J - \boldsymbol{R}_{IJ}|} \right] \,. \tag{3.4}$$

The seventh, eighth and ninth terms in Eq. (3.1) represent the contributions from the average electronic and nuclear charges outside the cluster. The last term in Eq. (3.1) is the exchange-correlation energy. Finally, it is important to appreciate that charge neutrality will always be restored after averaging over all the cluster configurations since the KKR-NLCPA is, by construction, a translationally invariant method.

The expression for the total energy in Eq. (3.1) is given in a general form, which is valid for ordered and disordered systems. In practice this formula has to be implemented according to the density and potential representations. In our method we use different approaches which makes the code flexible and adaptive for wide range of systems. Validity and advantages of these approaches will be discussed in the next chapter.

A new aspect of the total energy expression (3.1) is the Madelung energy (3.4) and the corresponding charge transfer effects, which are included self-consistently via the Madelung term of the crystal effective potential. Fig. 3.1 illustrates these effects in bcc $Cu_{50}Zn_{50}$ alloy. This system was investigated using the self-consistent KKR-NLCPA method for $N_c = 1$ (conventional CPA) and $N_c = 2$ (nonlocal CPA with 2 cluster sites). To analyze the effect of self-consistency we performed calculations of the DOS using nonlocal CPA approach for fixed potentials obtained with the conventional KKR-CPA method. The comparison of this DOS with the conventional CPA results is shown in Fig. 3.1(a). First note that there is little observable difference in the total DOS compared to the KKR-CPA calculations given in the same figure. This is expected as the size of the cluster is very small. Nevertheless, in a dramatic departure from the conventional KKR-CPA calculation where only single-site Cu and Zn components exist, here the component contributions from four possible cluster configurations are apparent. A self-consistent KKR-NLCPA DOS is presented in Fig. 3.1(b). It is clear that there is now an observable difference between the total DOS results obtained with the self-consistent KKR-NLCPA compared to the conventional CPA. This difference is plotted in Fig. 3.1(c) and integrates to zero since there are the same number of electrons per site in both cases. This difference arises from the charge transfer between the cluster sites at certain energy regions. Since $Cu_{50}Zn_{50}$ alloy is in the "split-band" regime, these energy regions are well separated and occur at places where the DOS has a large weight.
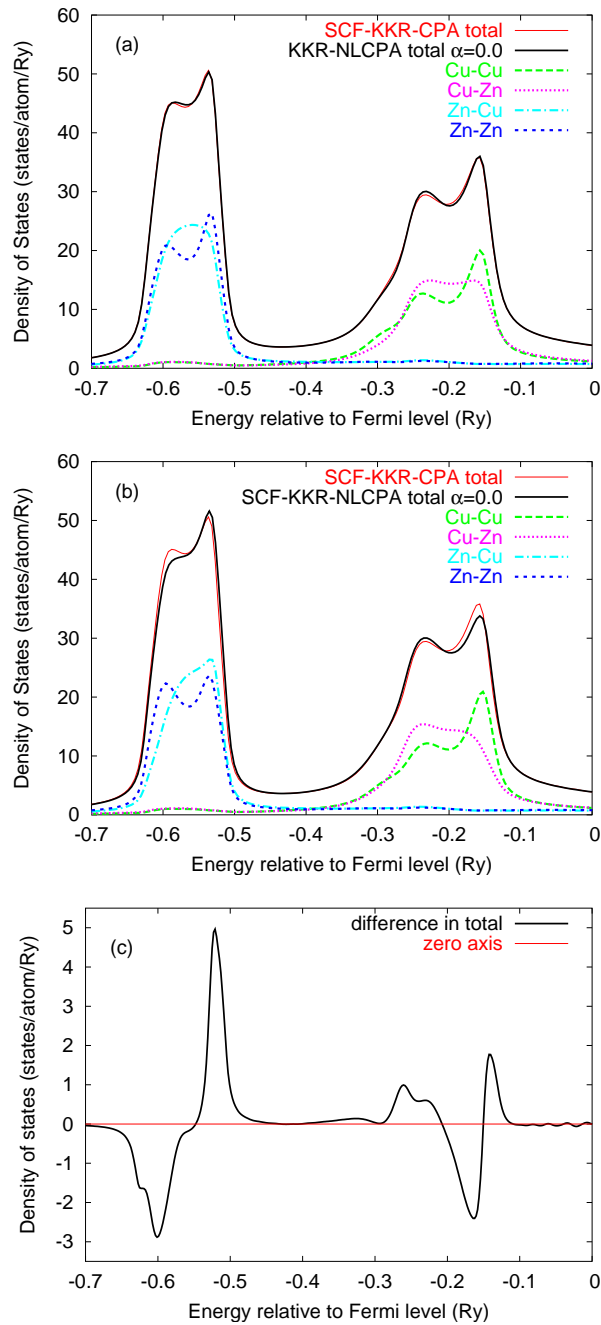
Figure 3.1. (a) Total average DOS for disordered $bcc\ Cu_{50}Zn_{50}$ using both KKR-CPA and KKR-NLCPA (non-SCF) with $N_c = 2$. Also shown are the contributions from the four possible cluster configurations measured at the first site-i.e., Cu for Cu-Cu, Cu-Zn, and Zn for Zn-Cu, Zn-Zn. (Owing to translational invariance, measurement at the second site would give the same results with a simple reversal of the labels.) (b) Same as above but using the new self-consistent filed SCF-KKR-NLCPA. (c) Plot of the difference between the total SCF-KKR-CPA and total SCF-KKR-NLCPA results.

Finally, there is a fairly obvious general comment to be made with regards to the total energy calculations within the multiple scattering theory. In contrast to any variational method, results obtained with the KKR Green function approach might be very sensitive to approximations and parameters, which have to be introduced by the implementation of the method. Any inconsistency with the formal multiple scattering theory can lead to a severe sacrifice in accuracy. Aspects of convergence of the KKR Green function will be discussed in the next section.

3.2. Convergence properties of the KKR Green function

The KKR Green function has always a proper asymptotic energy behavior due to its construction and can be in principle evaluated exactly at any energy, which makes this method attractive for the spectroscopy or applications in the many body physics. However, the analytical expression for the Green function (2.16) is exact in the limit of $L \to \infty$. In practice, the angular momentum summations in Eq. (2.16) are truncated at some reasonable l_{max} making the electronic wave function or the corresponding density of states to be only approximately normalized. This truncation error can lead to inconsistent results, especially in semiconductors or in applications requiring very accurate total energy calculations. Since the electronic wave functions are not normalized, the Fermi level cannot be determined accurately. In semiconductors the Fermi level is incorrectly placed in the valence band. Since the normalization error depends strongly on l_{max}, the Fermi level is not accurately determined and this leads to a slow convergence of the total energy with l_{max}. An additional error in the normalization arrises due to numerical integration of the Green function over the unit cell and energy in equations (2.41) and (2.42).

However, in the multiple-scattering theory the normalization can be achieved by applying the Lloyd formula (2.46) which allows the integrated density of states to be evaluated directly at any energy using only determinants of scattering matrices. The Lloyd formula increments the integrated density of states exactly by one every time the determinant of the secular matrix goes through zero regardless of the truncation in angular momentum. Thus, the integrated density of states (2.46) converges very rapidly with the angular momentum. The normalization of the truncated Green function (2.16) can be forced by multiplying with a factor

$$A(E) = \frac{N^{Lloyd}(E)}{\int\limits_{\infty}^{E} n(\varepsilon)d\varepsilon} \,, \tag{3.5}$$
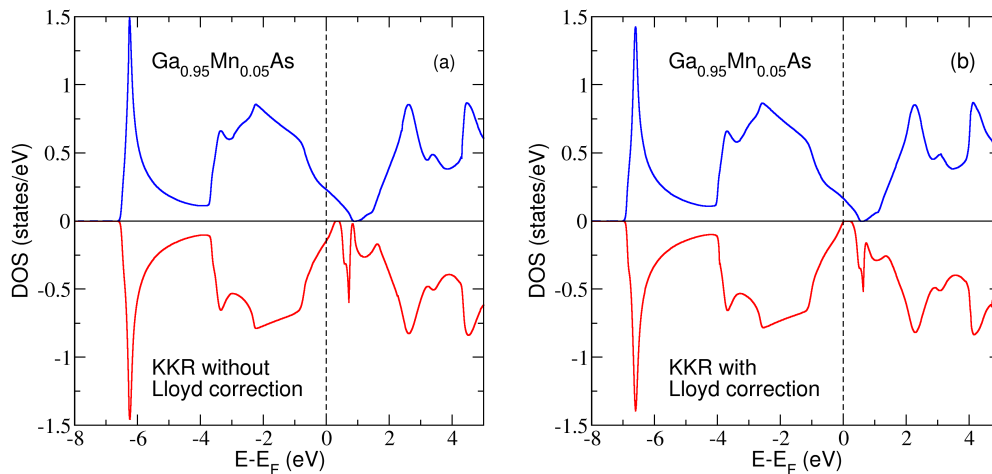
Figure 3.2. Total DOS of $Ga_{0.95}Mn_{0.05}As$ for the majority (blue line) and minority (red line) spin channels: (a) KKR-CPA without Lloyd correction; (b) KKR-CPA with Lloyd correction.

where $n(E)$ is the total density of states, Eq. (2.42), obtained from the truncated Green function (2.16). This procedure is similar to the normalization of basis functions in a variational method. This Lloyd correction can be applied as well on the charge density, so that it can be used in the self-consistency process. The efficiency of this normalization scheme is demonstrated in Fig. 3.2. In the left panel there is shown the spin-resolved total DOS of $Ga_{0.95}Mn_{0.05}As$ calculated from the truncated Green function (2.16) without any additional normalization. In both spin channels the DOS exhibits metallic behavior although it is well known as a half metal with an integer net magnetic moment per magnetic impurity. The Fermi level crosses the valence band in the minority spin channel where a band gap is expected. The estimated net magnetic moment $\mu = 3.26\mu_B$ is significantly lower than the expected one, namely $\mu = 4\mu_B$. Self-consistent inclusion of the Lloyd correction (3.5) provides the electronic structure (Fig. 3.2b) which is comparable with results obtained with other methods [87, 88]. The net magnetic moment is $\mu = 4\mu_B$ and there is a band gap in the minority spin channel.

In metals the truncation error is not so visible in the DOS as in semiconductors since the electronic states are partially occupied and, although, the Fermi level may not be correct but it does not occur in a principally wrong position. However, the truncation problem is general for any material, first of all, affecting the total energy. To demonstrate this fact we performed convergence tests for the total energy of copper. Copper is well studied with various first-principle methods. Since it has a close packed crystal structure and it is metallic, one expects rather fast convergence of the total energy with respect to the number of the basis functions. Our KKR results are presented in Fig. 3.3. For the tests we used different shape approximations for the potential representation. The results for the muffin-tin approximation are presented in panels (a) and (b). The convergence of the total energy without Lloyd correction (panel (a)) is non-systematic and can be explained by the fluctuation of the Fermi level. The curve for $l_{max} = 2$ is not even shown here because it falls completely out of the picture. The $l_{max} = 3$ curve is occasionally close to the results for $l_{max} = 6$, at which the total energy starts to converge. An acceptable accuracy is achieved at angular momentum truncation $l_{max} \geq 9$. The use of the Lloyd correction accelerates substantially the convergence of the total energy (panel (b)) and makes possible to perform accurate calculations already with $l_{max} = 3$ (see results for equilibrium lattice constants in Fig. 3.3(e)). The total energy converges absolutely for $l_{max} \geq 6$. The same convergence behavior of the total energy of copper is obtained using the full-charge density and full-potential approximations (the tests are not shown here because of the similarity). The muffin-tin, full-charge density and full-potential approximations give very similar results, because the interstitial region is narrow and non-spherical contributions to the total energy are negligible (at least for lattice constant calculations). Therefore, for close packed structures the MT approximation is quite reasonable and in many cases preferable due to numerical stability and simplicity.

In contrast to the MTA, another popular spherical potential approach, ASA, provides inadequate results within the KKR method. Without the Lloyd correction the equilibrium lattice constant is estimated to be 6% lower than the experimental one (Fig. 3.3(c)). Although the Lloyd correction improves continuously the convergence of the total energy, the error in the equilibrium lattice constant is still too large (Fig. 3.3(d)). The main reason for the failure of the ASA is the construction of this approximation, in which the atomic spheres overlap, that leads to incorrect scattering of electrons in the crystal. Thus, the KKR-ASA is completely inadequate for total energy calculations, although the DOS and spectral function, evaluated with the ASA, are visually comparable with the MTA or full potential results. The wrong scattering contribution can be corrected with the so-called ASA-MT approach [89]. It relies on overlapping atomic spheres for the calculation of the kinetic energy, similar to the atomic sphere approximation, however, a shape correction is used that has the same form as the interstitial treatment in the non-overlapping muffin-tin approach. The inter-site Coulomb energy is evaluated using the Madelung energy as computed in the MT approach, while the on-site Coulomb energy is calculated using the ASA.

Obviously, the representation for the crystal potential is an additional parameter in first principles calculations. More general is the full potential approximation, but unfortunately it can be very time consuming and not always numerically stable. Moreover, some applications, for instance, the self-interaction correction, are still not yet formulated in the full potential representation

and, therefore, it is desirable to have a method which has more choices for the potential shape. In the HUTSEPOT package there are implemented all established potential representations, which makes the code flexible and efficient for various applications in condensed matter physics. Validity of the implemented approximations is illustrated in Fig. 3.4. Here there are shown the errors in equilibrium lattice constants evaluated for several materials using the ASA, ASA-MTA, MTA and full-charge density (FCDA) approaches in the local density approximation. The full-potential results are very close to the FCDA and are omitted here.

The important conclusion following from these tests is that the atomic sphere approximation yields substantial error in the estimation of equilibrium lattice constants which is much larger than to be expected from the LSDA. The error becomes larger when the charge density has a larger weight in the overlapping region like in Ce, TiO_2 and manganese stabilized zirconia. However, it can provide reasonable results for structures with many atoms per unit cell by manipulating atomic radii as it was achieved in GaAs case shown in Fig. 3.4. The muffin-tin approximation seems to be adequate and efficient in close packed structures, especially for monoatomic unit cells. The combination of the ASA and MTA improves generally accuracy of the total energy calculations but for structures with large interstitial region it has a tendency to overestimate the equilibrium lattice constant.

Next, we consider the angular momentum convergence of magnetic properties calculated with the multiple-scattering theory. Many of these properties, such as Curie temperature and magneto-crystalline anisotropy, are usually estimated from the energy difference of various magnetic configurations, calculated at a fixed unit cell volume. As it was demonstrated above, the truncated multiple-scattering does not provide an absolute convergence of the total energy. If the total energy would have the same truncation error in different magnetic configurations, one can expect, the difference of the total energies would have a better convergence than the total energy itself. To verify this statement we investigated the angular momentum convergence of the local magnetic moment and Curie temperature of bcc iron. The calculations were performed self-consistently in ferromagnetic, antiferromagnetic and paramagnetic states using the muffin-tin approximation. The Curie temperature was estimated in the mean-field approximation from the difference of the total energies of ferromagnetic and paramagnetic configurations. The results of the truncated and Lloyd corrected KKR methods are presented in Fig. 3.5. The magnetic moments and Curie temperature, obtained with the truncated KKR method, have a very slow convergence behavior, while the Lloyd correction provides generally converged results with cut-off $l_{max} \geq 3$. A very interesting fact is, that the magnetic moments, calculated with the truncated KKR method, converge differently in different magnetic configurations. Obviously, it can be attributed to the single-scattering part of the Green function, because structure constants are potential independent and calculated practically on the same energy mesh (the Fermi level changes only slightly in these tests). This means that the convergence of the Green function depends strongly on the character of resonance states. In antiferromagnetic and paramagnetic cases 3d-resonances are more narrow than in ferromagnetic state. This affects the convergence of the Green function and leads to inconsistent results for the Curie temperature (Fig. 3.5(d)).

In the appended publications [P3,P4] we demonstrate the efficiency of our approach on electronic and magnetic structure studies of diluted magnetic semiconductors. In the reference [P3] we explain a photoemission experiment in the GaMnAs system, in which a weakly dispersive electronic band near the Fermi level is observed. We investigate the formation of this band which is closely related to the presence of the Mn interstitial impurities. In another study [P4], we propose the Mn-stabilized Zirconia as a new potential high-T_C ferromagnetic spintronics material. From the basis of ab initio electronic structure calculations which include the effects of thermally excited magnetic fluctuations, we predict Mn-stabilized cubic zirconia to be ferromagnetic above 500 K. We find this material, which is well known both as an imitation diamond and as a catalyst, to be half-metallic with the majority and minority spin Mn impurity states lying in zirconia's band gap.
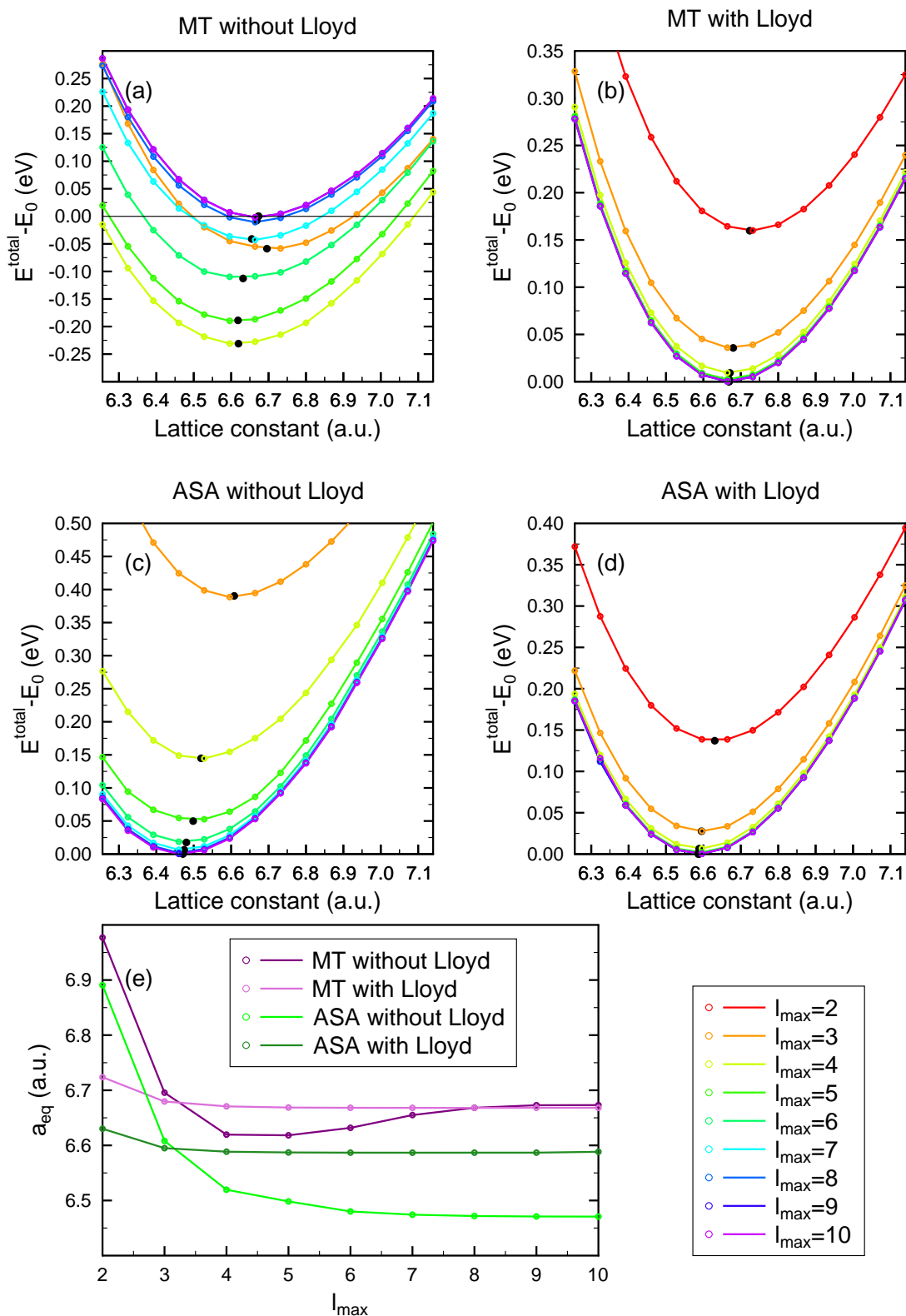
Figure 3.3. Convergence of the total energy of copper calculated using KKR-MTA and KKR-ASA with and without Lloyd correction. Equilibrium lattice constants are marked as black circles. Total energy vs. lattice constants: (a) KKR-MTA without the Lloyd correction, (b) KKR-MTA with the Lloyd correction, (c) KKR-ASA without the LLoyd correction, (d) KKR-ASA with the Lloyd correction. (e) Convergence of the equilibrium lattice constant with truncation angular momentum
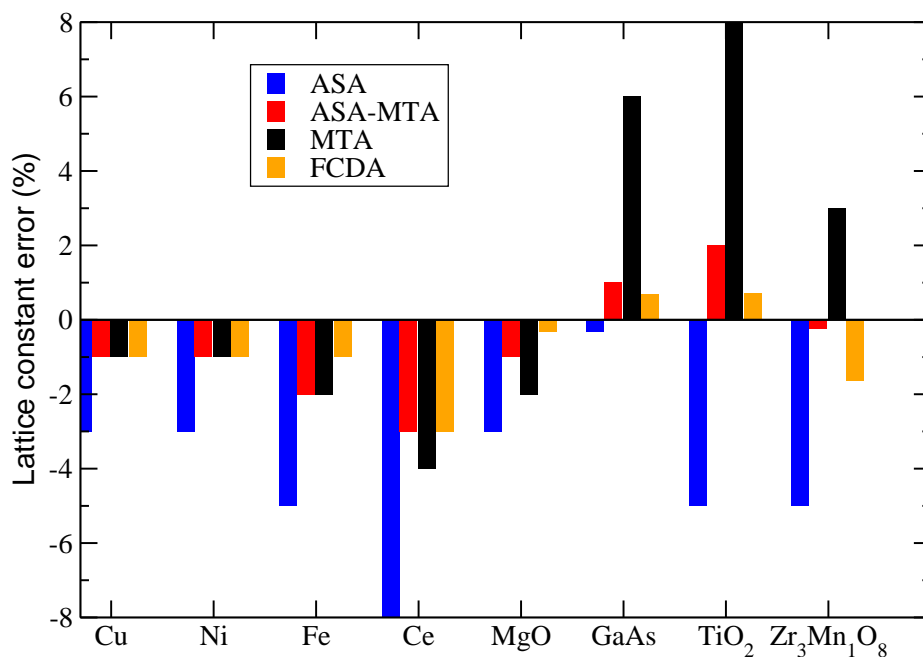
Figure 3.4. Error of estimated lattice constants for different materials using KKR method within the local density approximation
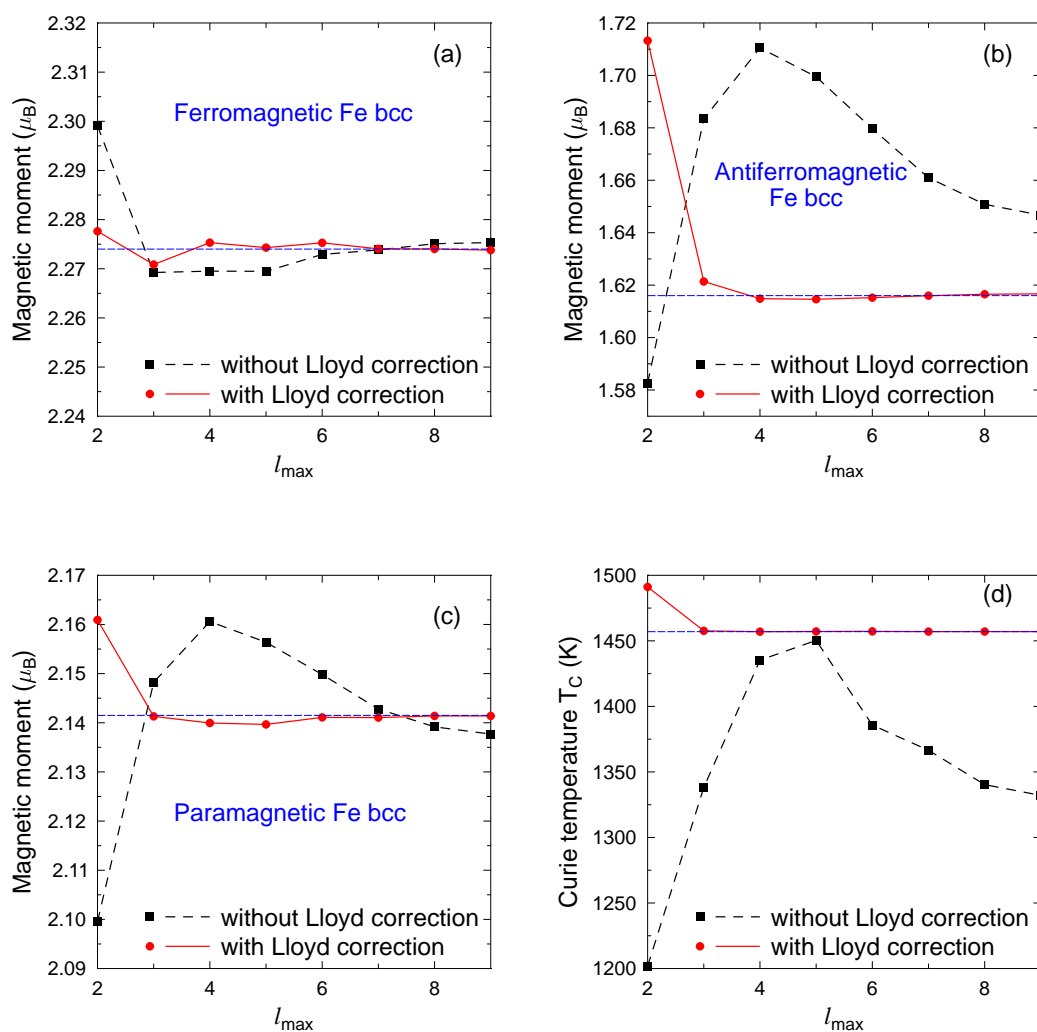
Figure 3.5. Angular momentum convergence of magnetic properties of Fe (bcc): (a) local magnetic moment in the ferromagnetic state, (b) local magnetic moment in the antiferromagnetic state, (c) local magnetic moment in the paramagnetic state, (d) mean-field Curie temperature.

3.3. Application: Electronic structure of $Mg_xZn_{1-x}O$ alloys

Due to slow convergence properties a truncated KKR method fails to describe correctly structural properties of low packing density systems. The Lloyd correction together with a full potential approximation make it possible to carry out a structural optimization of such systems. Here there is presented a study of structural properties of $Mg_xZn_{1-x}O$ alloys which can exhibit rock salt, hexagonal and wurtzite structures in accordance with the alloy composition.

In the recent years, much effort has been devoted to research on the $Mg_xZn_{1-x}O$ alloy systems due to their attractive properties for optoelectronic applications in ultraviolet region. Mostly, this interest arises from such properties of zinc oxide (hexagonal wurtzite structure) as a high piezoelectric coefficient, photoconductivity, and transparency in the visible and infrared ranges. The application field of this semiconductor can be considerably extended if it is alloyed with different concentrations of MgO (rock salt structure). This can enable varying the structure from the hexagonal wurtzite (WZ) to the rock salt (RS) phase and tuning the fundamental band gap from 3.25 to 7.7 eV.

To investigate phase transitions in $Mg_xZn_{1-x}O$ alloys, we used a scheme suggested for wurtzite-to-rock-salt transformation in GaN [90] and successfully applied to study structural deformations in MgO [91] and ZnO [92]. According to this scheme, the wurtzite-to-rock-salt transition can be described as a homogenous strain deformation from the wurtzite to the rock-salt by passing an intermediate hexagonal structure (HX), which the authors in [90] referred to as h-MgO. The first step occurs by linearly increasing the internal parameter u with continously decreasing the c/a ratio. At $u=1/2$ the space group changes from $P6_3mc$ to $P6_3/mmc$. Then, by uniaxial compressing along the $[10\bar{1}0]$ direction and decreasing the c/a ratio, the intermediate HX structure can be transformed to the rock-salt. The ideal crystal structure parameters for these three structures are presented in Table I in the Reference [91]. To perform the total energy minimization we used appropriate unit cells of an orthorhombic lattice with the space group $Cmc2_1$ (see Fig.3.6), which is a common subgroup for all these three structures [93]. In our calculations we fixed the parameter v and b/a which are determined by the geometry. The internal parameter u and c/a ratio were obtained by the energy minimization for pure ZnO and MgO compounds and chosen to be fixed for $Mg_xZn_{1-x}O$ alloys. The equilibrium volumes, bulk modulus, pressure and enthalpy were calculated at $T = 0$ from the total energy fitted to the Murnaghan equation. Lattice vibrations, finite temperature effects, relativistic corrections were not considered in the current work.

Pure MgO and ZnO   Due to the large number of internal parameters a full structure optimization of $Mg_xZn_{1-x}O$ alloys is quite a difficult task. Apart from usual structural parameters, the alloy composition is an additional degree of freedom, which complicates the problem furthermore. Therefore, we cut the number of variable parameters concentrating mostly on volume changes in WZ, HX and RS structures by varying the composition of the alloys. However, since the KKR method was never used for optimizations of wurtzite and hexagonal structures, we performed more extensive calculations for pure ZnO and MgO materials varying the internal parameter u and c/a ratio following the procedure suggested in Ref. [91]. The results for both zinc and magnesium oxides in the wurtzite and rock-salt structure, obtained with the KKR method, are presented in Table 3.1. There we have shown the main structural parameters, the equilibrium volumes, bulk modulus, equilibrium pressure, c/a ratio and internal parameter u, which are compared with experiments and some well established theoretical approaches: pseudo-potential plane waves (PPW), linear combination of atomic orbitals (LCAO) and FP-LMTO methods.

Since it is important to establish the validity of the KKR method for the structure optimization, we compare our results only with calculations performed within the density functional approximation, namely, the LSDA. It has to be mentioned that our simulations for both ZnO and MgO in various structures were carried out in the same unit cell on the same approximation level, while almost all presented results were obtained either for zinc or magnesium oxides. Generally, our calculations are in good agreement with experimental data and results of other theoretical approaches. A better agreement is achieved with all-electrons methods, especially with the works
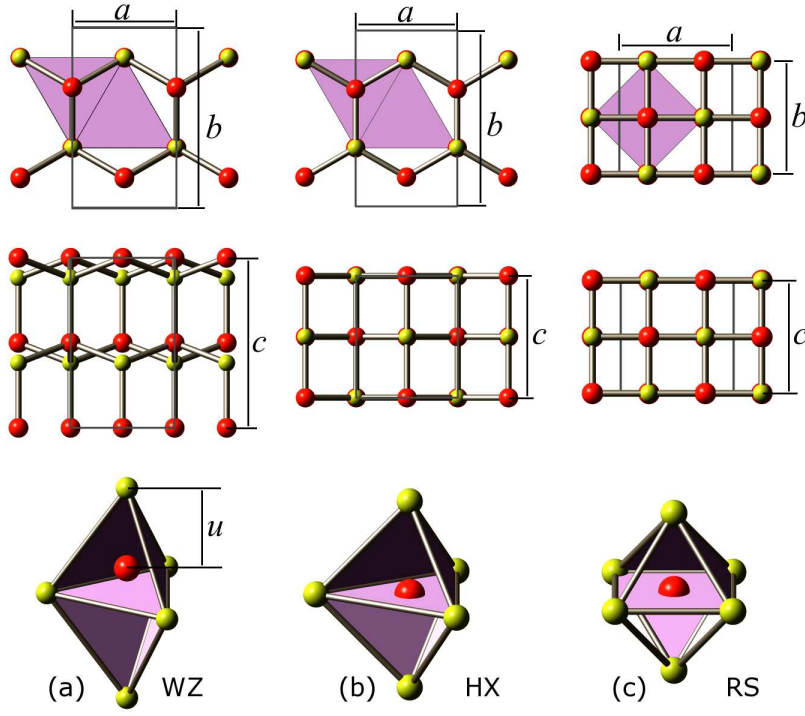
Figure 3.6. Views of WZ (a), HX (b) and RS (c) crystal structures.

of Limpijumnong and co-workers [91, 92]. A possible reason being that we performed structural optimizations applying the scheme suggested in those works. Also, the $3d$-electrons of zinc and $2p$-electrons of magnesium were treated in the same manner. Only the equilibrium pressure for the rock-salt-to-hexagonal phase transition in magnesium oxide does not agree well with the results obtained by Limpijumnong and co-workers. This can be related to the instability of MgO wurtzite and hexagonal structures, that can be responsible for discrepancies in various total energy calculations. Moreover, due to the negative pressure, the WZ and HX phases of pure MgO cannot be realized experimentally, which makes it impossible to compare theoretical results with experiment. A very important point is that our calculations reproduce well the c/a ratio and internal parameter u. Previous implementations of the multiple scattering theory were not able to optimize these structural parameters in open structures due to the slow angular momentum convergence of the Green function.

Mg$_x$Zn$_{1-x}$O   After establishing that our results for pure ZnO and MgO are consistent with the structural properties obtained with other methods and experiments, we have applied the same approach to study Mg$_x$Zn$_{1-x}$O alloys, using the CPA method. For that, we have fixed the c/a ratio and internal parameter u to the values of 1.6 and 0.38 in wurtzite structure and to the values of 1.2 and 0.5 in hexagonal structure, respectively, because we have found them depending weakly on the atom species (see Table 3.1). Therefore, varied are only the structure type, concentration of the atom species and volume of the unit cell. The results of our total energy calculations are summarized in Fig. 3.7. There we show the formation enthalpy of a structure α in Mg$_x$Zn$_{1-x}$O alloys

$$\Delta H_\alpha(\text{Mg}_x\text{Zn}_{1-x}\text{O}) = E_\alpha(\text{Mg}_x\text{Zn}_{1-x}\text{O}) - xE_{RS}(\text{MgO}) - (1-x)E_{WZ}(\text{ZnO}) \tag{3.6}$$

of a structure α in Mg$_x$Zn$_{1-x}$O alloys, taken relative to the most stable forms of ZnO (WZ) and MgO (RS) compounds, [104] with black lines marking the phase separations. It is seen that the formation enthalpy is positive for all volumes and concentrations. This is in agreement with previous theoretical studies of Mg$_x$Zn$_{1-x}$O, made with an accurate cluster expansion approach [96, 104]. There are two global minima, pure ZnO in wurtzite and pure MgO in rock-salt

structure, which means that the alloy has a tendency to phase separation when the integration of different constituents into the medium cannot be maintained [104].

Scanning with the CPA method the continuous range of concentrations, we have found generally five extremal cases: x_{Zn} =0.0, 0.29, 0.48, 0.67, 1.0 Four of them are presented in Fig. 3.8. In Fig. 3.8a the total energies of pure MgO (x_{Zn}=0.00) in different phases are shown. The rock-salt structure exhibits the global minimum at the volume of $18.19\,Å^3$/pair which is about 2% smaller than the experimental value (see Table 3.1). By applying a negative pressure along the tangent line the rock-salt phase is going to the hexagonal structure in agreement with the work of Limpijumnong and co-workers [91]. According to the phase diagram (Fig. 3.7), the hexagonal phase is always an intermediate phase between the rock-salt and wurtzite structures, at $0.00 \leq x_{Zn} \leq 0.67$. Although RS-to-HX transition pressure is increasing with the content of zinc, it remains negative at whole range of concentrations (see Fig. 3.9). At x_{Zn}=0.29 the rock-salt-to-hexagonal and from hexagonal-to-wurtzite transitions occur at the same pressure (Fig.3.8b). For $x_{Zn} > 0.67$ the total energy in the hexagonal structure is always higher than in rock-salt and wurtzite phases and a direct wurtzite-to-rock-salt transition at positive pressure is possible. At x_{Zn}=0.67 (see Fig. 3.8 and Fig. 3.10) this phase transition takes place at zero pressure, which is consistent with the work of Sanati and co-worker [104] and observed experimentally in ZnO-MgO hetero-structures [105]. With increasing the concentration of zinc, the wurtzite phase is always favorable and the pressure, which is needed for a wurtzite-to-rock-salt transition, is positive and rising continuously upwards (see Fig. 3.9). Finally, at $x_{Zn} = 0.48$ the HX-to-WZ transition is possible at zero pressure and the corresponding total energies relative to RS phase are the same (see Fig. 3.10).

Summarizing, we investigated the phase transition from wurtzite to rock-salt structure in $Mg_xZn_{1-x}O$. Comparing total energies of wurtzite, hexagonal and rock-salt structures, we found that the WZ phase is only stable for $x_{Zn} > 0.67$, which is in good agreement with experiment. For lower concentration of zinc a transformation from the rock-salt to wurtzite is possible by passing through intermediate hexagonal structure and applying a negative pressure. Calculated structural parameters of $Mg_xZn_{1-x}O$ alloys are generally in agreement with previous theoretical investigations and experiment. Thus, the Lloyd corrected KKR-CPA method within the full-charge density approximation provides an adequate description of binary alloys with low packing densities for whole range of concentrations.

Table 3.1. The equilibrium volumes V_0, c/a ratio, internal parameter u, bulk modulus B_0 and transition pressure P for pure ZnO and MgO, obtainted in current work and by various methods within the LSDA and compared with experiment.

	Current work	Other methods	Experiment
		ZnO, wurtzite structure	
V_0 (Å^3/pair)	22.83	22.80 [a], 22.87 [b], 23.78 [c], 22.93 [d]	23.81 [e], 23.80 [f]
c/a	1.602	1.610 [a], 1.614 [b], 1.605 [c], 1.617 [d]	1.602 [e], 1.602 [f]
u	0.381	0.380 [a], 0.379 [b], 0.380 [d]	0.382 [e], 0.382 [f]
B_0(GPa)	154	162 [a], 162 [b], 154 [c], 162 [d]	143 [e], 183 [f]
		ZnO, hexagonal structure	
V_0 (Å^3/pair)	22.12		
c/a	1.200		
B_0(GPa)	165		
		ZnO, rock-salt structure	
V_0 (Å^3/pair)	18.88	18.70 [a], 18.98 [b], 19.45 [c], 18.87 [d]	19.60 [e], 19.48 [f]
B_0(GPa)	201	210 [a], 206 [b], 200 [c], 211 [d]	202 [e], 228 [f]
		phase transitions in ZnO	
V_{WZ}/V_{RS}	1.21	1.22 [a], 1.20 [b], 1.22 [c], 1.22 [d]	1.21 [e], 1.22 [f]
$P_{WZ \to RS}$ (GPa)	8.6	8.2 [a], 6.6 [b], 8.0 [c], 8.7 [d]	9.1 [e], 8.7 [f]
		MgO, wurtzite structure	
V_0 (Å^3/pair)	23.41	22.53 [c], 22.50 [gg]	
c/a	1.601	1.550 [c], 1.620 [g]	
u	0.380	0.380 [g]	
B_0(GPa)	121	131 [c], 137 [g]	
		MgO, hexagonal structure	
V_0 (Å^3/pair)	21.71	20.90 [g]	
c/a	1.200	1.200 [g]	
B_0(GPa)	135	148 [g]	
		MgO, rock-salt structure	
V_0 (Å^3/pair)	18.19	18.03 [b], 17.54 [d], 17.80 [g], 18.65 [h]	18.67 [i], 18.75 [j]
B_0(GPa)	167	186 [b], 170 [c], 178 [g], 172 [h]	172 [i], 169 [k]
		phase transitions in MgO	
V_{HX}/V_{RS}	1.19	1.17 [g]	
$P_{RS \to HX}$ (GPa)	-8.5	-16.2 [g]	
V_{WZ}/V_{RS}	1.24	1.28 [d], 1.26 [g]	
$P_{RS \to WZ}$ (GPa)	-11.1	-8.4 [g]	

[a]Reference [92]: PPW
[b]Reference [94]: LCAO
[c]Reference [95]: PPW
[d]Reference [96]: PPW
[e]Reference [97]
[f]Reference [98]
[g]Reference [91]: FP-LMTO
[h]Reference [99]: FP-KKR
[i]Reference [100]
[j]Reference [101]
[i]Reference [102]
[k]Reference [103]

Enthalpy per formula unit (eV)
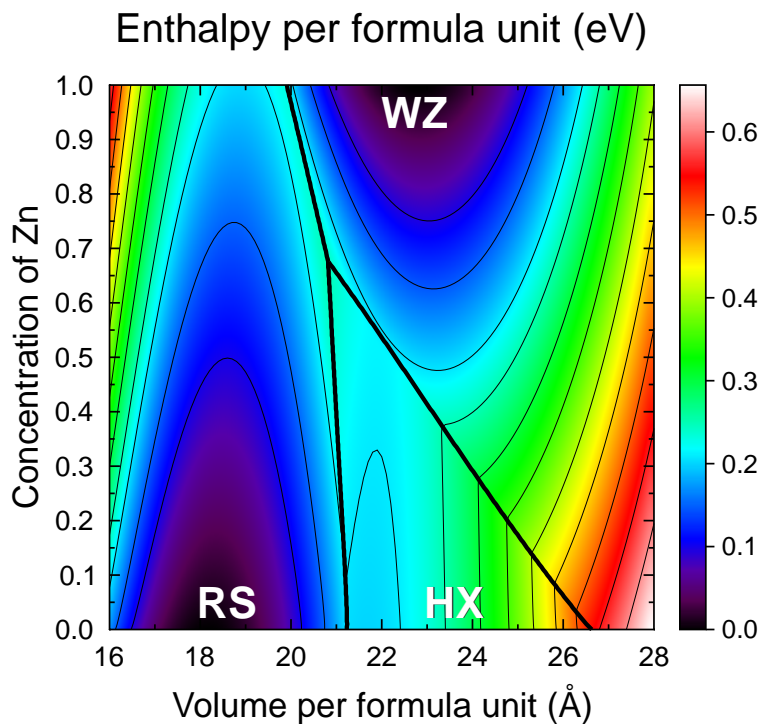
Figure 3.7. Formation enthalpy of $Mg_xZn_{1-x}O$ alloys.
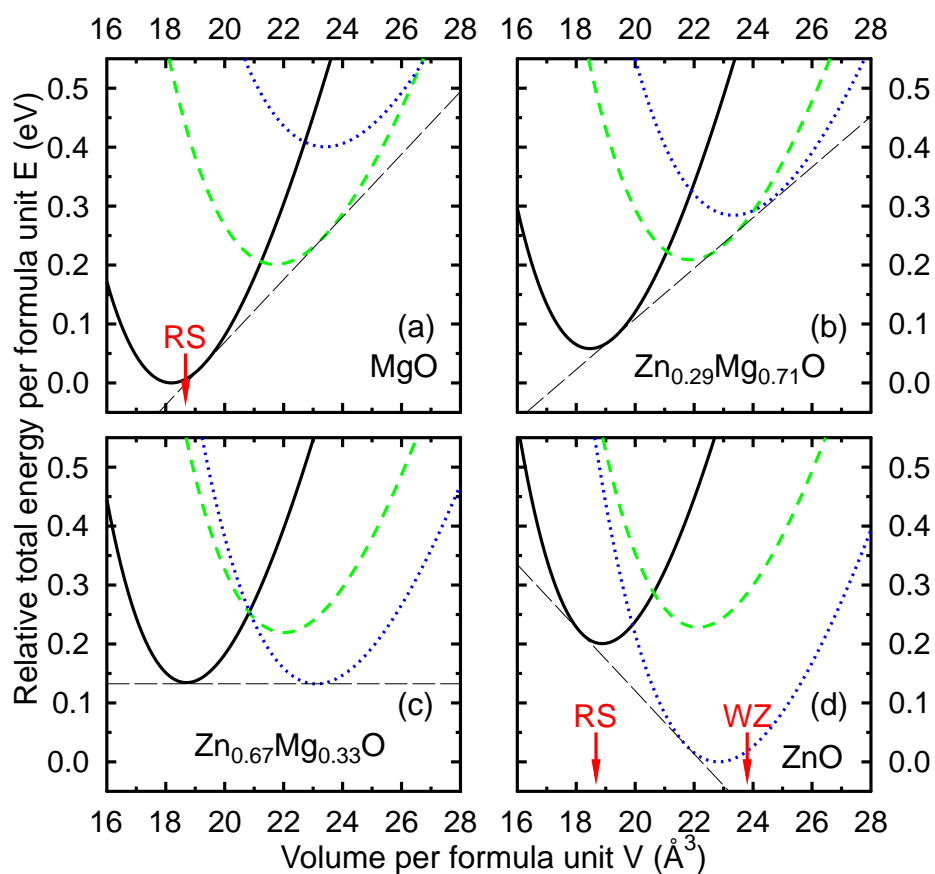
Figure 3.8. Relative total energies of $Mg_xZn_{1-x}O$ alloys in rock-salt (black solid line), hexagonal (green dashed line) and wurtzite (blue dotted line) structures at four different concentrations: (a) x_{Zn}=0.0 (pure MgO), (b) x_{Zn}=0.29, (c) x_{Zn}=0.67, (d) x_{Zn}=1.0 (pure ZnO). Total energies in cases (a), (b) and (c) are taken relative the RS phase at x_{Zn}=0.0 and in (d) – relative the WZ phase at x_{Zn}=1.0
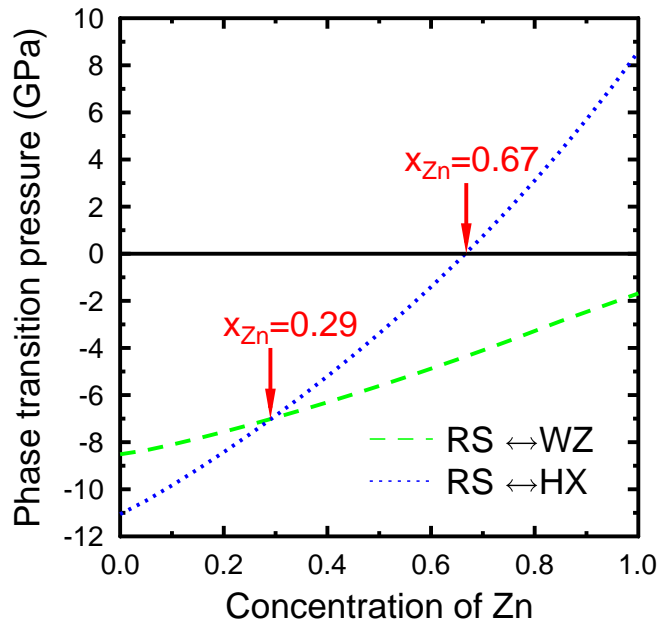
Figure 3.9. Equilibrium pressure in $Mg_x Zn_{1-x}O$ alloys: RS↔WZ (green dashed line) and RS↔HX (blue dotted line).
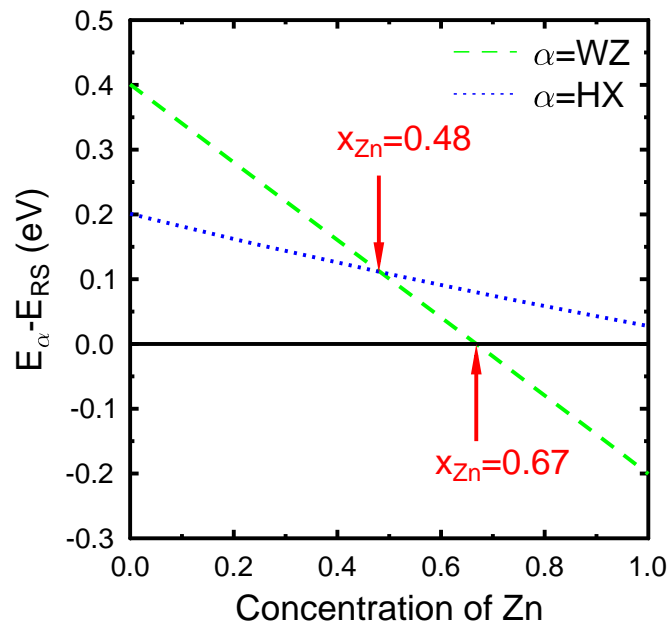
Figure 3.10. Total energies of $Mg_x Zn_{1-x}O$ alloys in hexagonal (blue dashed line) and wurtzite (green dotted line) structures taken relative the total energy of rock-salt structure at equilibrium volumes.

4. Multiple scattering theory for correlated systems

Most first principles calculations of condensed matter systems are based on density functional theory in the local spin density approximation. While for many materials this is an excellent approach, it fails for a class of systems containing localized d- or f-electrons which are characterized by strong correlation effects. The origin of these correlations is a strong Coulomb interaction, which can not be correctly taken into account by the LSDA, since it is designed for systems with itinerant electrons. A useful scheme to describe the static limit of these correlations is the self-interaction corrected local spin density approximation (SIC-LSDA) [106, 107]. In particular, it can determine whether an electron is delocalized or localized, i.e. whether its orbital is a part of valence state or not. This leads to a determination of the number of valence states and a nominal valence, as demonstrated by numerous calculation on rare earth, actinides, transition metal oxides (TMO), including the parent compounds of the high T_C materials and materials exhibiting a colossal magnetoresistance [108–114].

The full SIC-LSD scheme is unfortunately difficult to implement [115]. This is due to repeated transformations from reciprocal space (k-space) to real space to evaluate the self-interaction potential and the back transformation to k-sapce to solve the band-structure problem. So far most applications of the full SIC formalism have been implemented in the LMTO-ASA band-structure method [9]. A simpler scheme could lead to a new functionality and applications such as an inclusion of dynamical valence and spin fluctuations or an alloy description with the coherent-potential approximation.

Motivated by these aims we have developed a new single-site SIC-LSD approach [P5], referred to as local self-interaction (LSIC) formalism, which is an approximation to the full approach, but implemented in the multiple scattering theory. It is based on the experience that more than 98% of the electron is localized on the site under consideration. A localized state has a very sharp resonance in its phase shift, associated with a large Wigner-delay time on a particular site. This allows us to make a single-site approximation to determine the SIC charge density and the SIC potential.

One of the advantages of the multiple-scattering implementation of the SIC-LSD formalism is that it can be easily generalized to include the coherent potential approximation, extending the range of applications to random alloys. In addition, one can use it to treat static correlation beyond the LSDA by studying pseudoalloys whose constituents are composed e.g. of two different states of a given system: one delocalized, described by the LSD potential, and another localized, corresponding to the SIC-LSD potential. Combined with the disordered local moment (DLM) formalism for spin fluctuations [43], this allows also for different orientations of the local moments of the constituents involved.

4.1. Self-interaction in multiple scattering theory

It has been pointed out by Perdew and Zunger [59] that density functional theory schemes, like the local spin density approximation, suffer from a spurious self-interaction of the electrons. In principle, this self-interaction term should vanish exactly, as it does in the Hartree-Fock theory. In practice, however, this cancellation is incomplete. Perdew and Zunger suggested an approximate solution to this problem, which was constructed for finite systems but is here extended to solids in a novel way as compared to previous implementations for solids [115, 116].

The usual representation of the total energy within the LSDA-DFT formalism in the Kohn-Sham

approach [117] is

$$
\begin{aligned}
E^{\mathrm{LSDA}}[n_\uparrow, n_\downarrow] &= \sum_{\alpha\sigma}^{\mathrm{occ}} \langle \phi_{\alpha\sigma}| -\nabla^2 |\phi_{\alpha\sigma}\rangle + E_{\mathrm{ext}} \\
&\quad + E_{\mathrm{H}}[n] + E_{\mathrm{xc}}^{\mathrm{LSDA}}[n_\uparrow, n_\downarrow],
\end{aligned}
\tag{4.1}
$$

where $\phi_{\alpha\sigma}$'s are the Kohn-Sham orbitals, ($\alpha\sigma$ is a combined index labeling the orbital and spin ($\uparrow$ or $\downarrow$), respectively), $n_{\alpha\sigma} = |\phi_{\alpha\sigma}|^2$, $n_\sigma = \sum_\alpha^{\mathrm{occ}} n_{\alpha\sigma}$, $n = n_\uparrow + n_\downarrow$. E_{ext} is the external potential energy functional, E_{H} is the Hartree energy

$$
E_{\mathrm{H}}[n] = \int \mathrm{d}\boldsymbol{r} \int \mathrm{d}\boldsymbol{r}' \, \frac{n(\mathbf{r})n(\mathbf{r}')}{|\mathbf{r}-\mathbf{r}'|}, \tag{4.2}
$$

and $E_{\mathrm{xc}}^{\mathrm{LSDA}}$ is the LSD approximation to the exchange-correlation energy functional. On the basis of the above, Perdew and Zunger proposed a self-interaction corrected LSDA energy functional on an orbital by orbital basis

$$
\begin{aligned}
E^{\mathrm{SIC-LSDA}}[\{n_{\alpha\sigma}\}] &= \tilde{E}^{\mathrm{LSDA}}[n_\uparrow, n_\downarrow] - \\
&\quad - \sum_{\alpha\sigma}^{\mathrm{occ}} (E_{\mathrm{H}}[n_{\alpha\sigma}] + E_{\mathrm{xc}}^{\mathrm{LSDA}}[n_{\alpha\sigma}, 0]),
\end{aligned}
\tag{4.3}
$$

by subtracting explicitly the self-Coulomb and self-exchange and self-correlation energy of all *occupied* orbitals. $\tilde{E}^{\mathrm{SIC-LSDA}}[n_\uparrow, n_\downarrow]$ is of the same structure as $E^{\mathrm{LSDA}}[n_\uparrow, n_\downarrow]$ but with the orbitals $\phi_{\alpha\sigma}$ minimizing the self interaction corrected energy. This correction restores the property that the true functional $E[n]$ should have, namely that the self-Coulomb energy exactly cancels the self-exchange and self-correlation energy for every single orbital, $E_{\mathrm{H}}[n_{\alpha\sigma}] + E_{\mathrm{xc}}^{\mathrm{exact}}[n_{\alpha\sigma}, 0] = 0$. It leads to an orbital dependent SIC-potential seen by an electron in orbital $\phi_{\alpha\sigma}$,

$$
\begin{aligned}
V_{\mathrm{eff},\alpha\sigma}^{\mathrm{SIC-LSDA}}(\mathbf{r}) &= \underbrace{V_{\mathrm{ext}}(\mathbf{r}) + V_{\mathrm{H}}[n](\mathbf{r}) + V_{\mathrm{xc}\sigma}^{\mathrm{LSDA}}[n_\uparrow, n_\downarrow](\mathbf{r})}_{V_{\mathrm{eff},\sigma}^{\mathrm{LSDA}}} \\
&\quad - \underbrace{V_{\mathrm{H}}[n_{\alpha\sigma}](\mathbf{r}) - V_{\mathrm{xc},\sigma}^{\mathrm{LSDA}}[n_{\alpha\sigma}, 0](\mathbf{r})}_{V^{\mathrm{SIC}}(\mathbf{r})},
\end{aligned}
\tag{4.4}
$$

with the external lattice potential $V_{\mathrm{ext}}(\mathbf{r})$, and

$$
V_{\mathrm{H}}[n](\mathbf{r}) = 2 \int \mathrm{d}\boldsymbol{r}' \, \frac{n(\mathbf{r}')}{|\mathbf{r}-\mathbf{r}'|}, \tag{4.5}
$$

$$
V_{\mathrm{xc},\sigma}^{\mathrm{LSDA}}[n_\uparrow, n_\downarrow](\mathbf{r}) = \frac{\delta E_{\mathrm{xc}}^{\mathrm{LSDA}}[n_\uparrow, n_\downarrow]}{\delta n_\sigma}. \tag{4.6}
$$

This self-interaction correction vanishes exactly for extended states. In order to apply the SIC scheme to solids, the approach by Perdew and Zunger has to be generalized. This is achieved by introducing localized Wannier orbitals, for which the SI correction remains finite. In general, both localized and delocalized states lead to a local minimum of the SIC-LSD energy functional. The choice of states which have to be self interaction corrected is not unique. Therefore different configurations of such states have to be tested to find the one with the lowest energy which defines the ground state. For each configuration, one can define the valency by

$$
N_{val} = Z - N_{core} - N_{SIC} \tag{4.7}
$$

where Z is the atomic number, N_{core} is the number of core (and semicore) states and N_{SIC} is the number of localized or self-interaction corrected states.

The generalization of the Perdew and Zunger idea used in our formalism is based on the notion of resonances in scattering theory, which are the reminiscence of atomic states in the solid [P5]. Core states are represented by bound states at negative energies, where the imaginary part of the generalized complex phase shift jumps abruptly by π. Localized valence states still have very sharp resonances but band-like states are characterized by slowly varying phase shifts. In order to remove the spurious self-interaction we consider the problem of electrons moving in an array of scatterers. As already mentioned, an electron which shows localized behavior has a sharp resonance in its phase shift, associated with a large Wigner-delay time on a particular site. To determine the SIC charge we will consider for a moment the atomic limit, i.e., the situation where the scatterers are far apart. In this case the single site t-matrix and the local multiple scattering τ-matrix coincide, and all occupied states correspond to bound states. In this limit each bound state contributes exactly the charge of one electron, and this charge can be calculated by integrating the diagonal of the spectral function just around the energy of the bound state. In order to be able to decompose the charge density (Eq.(2.41)) into distinguishable channels, which reflect the crystal symmetry of the system, we choose symmetry adapted spherical harmonics. They are defined by applying a unitary transformation to the ordinary real (or complex) spherical harmonics, such that the on-site scattering matrix becomes diagonal. In order to be consistent with the muffin-tin or atomic sphere approximation, we only keep the spherical part of the channel densities. In this case, the local $\underline{\tau}^{ii}$ matrix becomes diagonal in symmetry adapted spherical harmonics. Different l belong to different irreducible representations. Therefore it is sufficient to consider each l block separately and to diagonalize the submatrices with given angular momentum separately. This defines a so called *channel* labeled by $\tilde{L} = (l, \tilde{m})$ which we use for the correction. In the following we denote the representation were the local τ matrix is diagonal by using indices with a tilde. In general this channel is a linear combination of the original angular momentum channels.

$$\sum_{m_1,m_2} U^\dagger_{(l\tilde{m},lm_1)}\underline{\tau}^{ii}_{(lm_1,lm_2)}(\epsilon)\, U_{(lm_2,l\tilde{m}')} = \delta_{\tilde{m}\tilde{m}'}\tilde{\underline{\tau}}^{ii}_{l\tilde{m}}(\epsilon) =: \underline{\tau}^{ii}_{\tilde{L}}(\epsilon)\,. \tag{4.8}$$

The regular solution transforms to a solution representing the channel:

$$Z^i_{\tilde{L}\sigma} = Z^i_{l\tilde{m}\sigma}(\boldsymbol{r}_i;\epsilon) = \sum_{m1} U^\dagger_{(l\tilde{m},lm_1)} Z^i_{lm_1\sigma}(\boldsymbol{r}_i;\epsilon) \tag{4.9}$$

and the other functions (e.g. $J^i_{\tilde{L}\sigma}$) respectively. It is easy to verify that the required transformation matrix U is, in fact, independent of the energy ϵ. This transformation to symmetry adapted spherical harmonics also ensures that the degeneracy of states, which are localized, is conserved. In this symmetrized representation, the Green's function becomes diagonal with respect to this quantum number. Hence we can decompose the spin resolved charge density into its $\tilde{L}$ components and define the charge of a state, characterized by its principle quantum number n, angular momentum $\tilde{L}$ and spin σ:

$$n^{\mathrm{SIC}}_{n\tilde{L}\sigma}(\boldsymbol{r}) = -\frac{1}{\pi}\int_{E_1}^{E_2} \mathrm{d}\epsilon\, \mathrm{Im}G_{\tilde{L},\sigma}(\boldsymbol{r},\boldsymbol{r};\epsilon), \tag{4.10}$$

where the energies E_1 and E_2 lie slightly below and above the energy of the state $nL\sigma$. The integration should enclose only the localized state, but for simplicity we use the usual valence contour, ranging from the bottom of the valence band to the Fermi energy.

The charge density, calculated in the proposed way, is used to construct the effective self-interaction free potential $V^{\mathrm{SIC-LSDA}}_{\mathrm{eff},i\tilde{L}\sigma}(\boldsymbol{r})$ from Eq. (4.4). In our approach we only consider the spherically symmetric part of the SIC density and SIC potential. Hence, each of these $\tilde{L}$ dependent potentials gives rise to a t-matrix which is is diagonal in l and $\tilde{m}$. Formally, these l-dependent spherical potentials can be combined in the form of a semi-local potential:

$$V(\boldsymbol{r},\boldsymbol{r}') = \sum_{\tilde{L}} Y^*_{\tilde{L}}(\hat{\boldsymbol{r}})\delta(r-r')V_{\tilde{L}}(r)Y_{\tilde{L}}(\hat{r}')\,. \tag{4.11}$$

Such potential gives rise to a diagonal t-matrix, where each matrix element $t_{\tilde{L}}$ corresponds to the spherical potential $V_{\tilde{L}}(r)$. The single-site scattering matrix including the self-interaction correction of some channels can be written as:

$$t^{i,corr}_{\tilde{L}\sigma} = t^i_{\tilde{L}\sigma}(1 - \delta_{\tilde{L},\tilde{L}^c}\delta_{\sigma,\sigma^c}) + t^{i,\mathrm{SIC-LSDA}}_{\tilde{L}^c\sigma}\delta_{\tilde{L},\tilde{L}^c}\delta_{\sigma,\sigma^c}, \tag{4.12}$$

where $t_{\tilde{L}\sigma}^{i}$ is the t-matrix calculated from the effective potential $V_{\text{eff},\sigma}^{\text{LSDA}}(\boldsymbol{r})$, and $t_{\tilde{L}\sigma}^{i,\text{SIC}-\text{LSDA}}$ is calculated from the SI-corrected potential $V_{\text{eff},i\tilde{L}\sigma}^{\text{SIC}-\text{LSDA}}(\boldsymbol{r})$. This corrected t^{corr}-matrix is then used in Eq.(2.17) to calculate the new, SI-corrected, scattering path matrix $\underline{\tilde{\tau}}$. From the latter the new SIC-LSDA charge density is calculated, and the process is iterated until self-consistency is reached.

The multiple scattering SIC approach is discussed in details in the attached publication [P5]. In this paper, we introduce the formalism of the local SIC approximation within the multiple scattering theory and illustrate this method on the application to the Ce α-γ transition. Ce, being the first element containing an f electron, has an interesting phase diagram, showing, in particular, the iso-structural (fcc–fcc) α-γ phase transition which is associated with a 15–17% volume collapse and quenching of the magnetic moment. In order to describe the ground state properties of Ce, we have calculated the total energy for different volumes using the LSDA approach for α-phase and the SIC formalism with correcting one f-electron, occupying in sequence all possible f-states, for γ-state. The ground state properties of Ce are generally in good agreement with experiments, demonstrating the applicability of the SIC formalism. At finite temperature we describe Ce as a pseudo-alloy of α and γ-Ce atoms. The calculated critical temperature overestimates the experimental one by a factor of two, which is still reasonable considering that the critical temperature is very sensitive to various details of the calculation. The slope of the phase separation line is in very good agreement with the experiment. In the paper we discuss as well many methodological aspects of the multiple scattering SIC approach and propose a roadmap for the development of the method towards the dynamical mean-field theory.

In the next publication [P6], we apply the self-interaction correction together with the DLM approach for the magnetic susceptibility [44, 45] to investigate magnetic and structural properties of heavy rare earth elements. Using gadolinium as a prototype for all heavy rare elements, we generate a unified magnetic phase diagram, which links the magnetic structures of the heavy rare earth to their lattice parameters and c/a ratio. In addition, we discover that the well known "lanthanide contraction" plays a separate, completely distinct role in determining the magnetic properties of the heavy rare earths.

4.2. Application: Electronic structure of transition metal oxides

The $3d$ transition metal oxides (TMO's) exhibit a rich variety of electronic and magnetic phenomena, and they have attracted a lot of attention over the last decades, in particular concerning the nature of the band gap and the excitation spectrum in general. In the ground state the TMO's crystallize in the rock-salt structure and exhibit antiferromagnetic ordering of type 2 (AF II), with planes of opposite spins being repeated in alternating order along the [111] direction, defining two sublattices consisting of spin-up and spin down metal ions, respectively. The TMO's are Mott-Hubbard insulators (some of them are also of charge-transfer type) and belong to the class of strongly correlated systems. The origin of correlations in TMO's is a strong Coulomb-repulsion on the transition metal sites, which leads to localisation of electrons and insulating behavior even though the d-bands are partially filled. Due to the highly correlated nature of the electron interaction in the TMO's, theoretical investigations employing first-principles methods to describe the electronic structure of these materials are difficult. The LSD approximation fails to describe correctly certain properties of these oxides, predicting too small magnetic moments and gaps or even metallic behavior for CoO and FeO. Several approaches beyond the LSD approximation have been applied for a realistic description of the TMO's. Among them is the LDA+U method [118], which achieves an effective Hubbard-splitting of d-bands using an effective Hubbard-U parameter. Another promising method appears to be the LDA-DMFT approach, which combines band structure and many-body theory, the dynamical mean field theory (DMFT)[119]. However, these methods suffer from uncertainty of the external parameter U, which is difficult to obtain from first-principles. In contrast to these methods, the SIC-LSD approach provides indeed a parameter free *ab-initio* description for the electronic structure of the TMO's. Several investigations of TMO's within the SIC approximation have been made during the last decades [61, 120, 121]. Applying this approach to TMO's yields an improved electronic structure of these compounds which is then
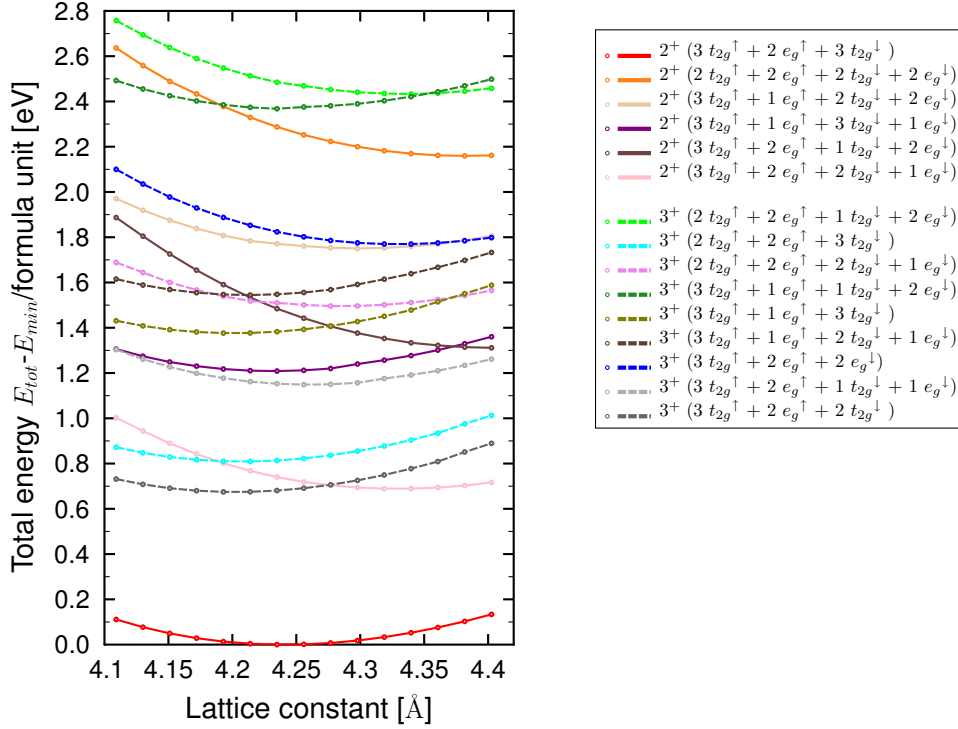
Figure 4.1. Total energies of different SIC configurations of NiO calculated in dependence of the lattice constant for all possible 2^+ and 3^+ configurations, which are labeled by their local symmetry, namely t_{2g} and e_g. The energy zero is set to the 'global' minimum of the different configurations. The lowest energy was found for the high symmetry state where 8 d-channels are corrected (Ni has 8 d-electrons) with valency 2^+.

manifested in magnetic moments and band gaps which are in accord with experiments. All these calculations have been done with the full SIC-LSD LMTO implementations. The main goal of the current study is to demonstrate the validity of the LSIC approximation on the TMO's comparing the LSIC results with previous studies and experiment.

Prototypical TMO: NiO. For a detail comparison of the SIC-LSD KKR method with SIC-LSD LMTO implementations, we chose NiO as a prototypical transition metal oxide, which was extensively studied both with theory and experiment. In order to find the absolute minimum of the SIC-LSD functional, one has to explore various manifolds of localized and delocalized states. To determine the valence configuration we performed total energy calculations of all possible configurations localizing particular electron ($3d$-)states by applying to these the SI corrections. In agreement with [120] and [61] we found the lowest total energy corresponding to the Ni valency of 2^+, when all d-electrons in one channel and 3 t_{2g} electrons in another spin channel are localized and have to be SI corrected. This corresponds to fullfiling the first Hund's rule (maximizing the spin moment). Any other configuration has a higher total energy (see Fig. 4.1). Single-scattering properties of a nickel site and NiO density of states corresponding to the lowest total energy configuration are demonstrated in Fig. 4.2. In Fig. 4.2(a) the shifts for the SI corrected and uncorrected d channels of Ni are shown. It can be seen that the uncorrected d states have a very sharp resonance just below the Fermi level. The steep resonance corresponds to a long Wigner delay time and indicates the state is already well localized. The self-interaction corrected d states are split according to the crystal symmetry and shifted down in energy by about 10 eV. The corresponding resonances are getting sharper, so the SI corrected d channels become bound states. The uncorrected d states are effectively shifted upwards so that the band gap opens up (the corresponding total DOS and d projected contributions are shown in Fig. 4.2(b).

The density of states of NiO, calculated with the SIC-LSD KKR method, is in good agreement with results, obtained with the full SIC-LSD LMTO implementation [61]. This can be seen in Fig. 4.3. There we present the NiO DOS, estimated with both implementations, and compare them with the LSD KKR calculations. Since we use the KKR method, it is not expected to get a full agreement with the SIC-LSD LMTO calculations, especially regarding the position of the SIC corrected Ni-d states, but they are very similar. Other properties to compare are the band gap and the local spin moment, see the table 4.1.

TMO series. We extended our studies to the series on TMO's which occur in the rock-salt AF II as discussed in the beginning of this section. The results in comparison to [61, 120] are shown in table 4.1. Figure 4.4 shows a significant improvement of the SIC-LSD calculations of the equilibrium lattice constant, local magnetic moment and the band gap in comparison to the LSD approach. For all TMO's the equilibrium lattice constants, obtained within the LSD approximation, are too small, while our SIC-LSD calculations overestimate them slightly and show the correct trend over the whole series. The same trend can be seen for local magnetic moments on the transition metals, which are getting larger in comparison to the LSDA results and are in good agreement with the experimental values except for CoO (this is due to not taking spin orbit coupling into account which will increase the moment). Our local moments are comparable as well to results obtained with the full SIC-LSD LMTO implementations. Applying the SIC-LSD approach increase systematically the size of band gaps for all TMO's. However, the band gap is an excited state property and can not be correctly described with the SIC-LSD method, since the latter is designed for description of the ground state.

In summary, we demonstrated the efficiency of the LSIC approach on the study of electronic properties of transition metal oxides. Our results are in very good agreement with results obtained with existing full SIC-LSD LMTO implementations and experiment. This fact demonstrates the validity of the simplified SIC approximation, and opens new possibilities for electronic structure studies of correlated systems. Its great potential, and in some way superiority, arises from the local and multiple-scattering aspects through which the method lends itself easily to various generalizations and extentions on the account of the straightforward determination of the one-electron Green function.

Table 4.1. Lattice constants, local magnetic moments and the band gaps for the series of transition metal oxides of our implementation, two other implementations and the corresponding experimental values. The values in round brackets for the magnetic moment are calculated at the experimental lattice constant. Our results compared to the experimental values can be seen in figure 4.4.

| | Compound | | | | |
	MnO	FeO	CoO	NiO	CuO
lattice constant [Å]					
LSD KKR	4.22	4.17	4.04	3.98	4.08
SIC-LSD KKR	4.45	4.39	4.31	4.24	4.27
Expt.	4.446[122],4.44[123]	4.326[124]	4.26[123, 125]	4.176[126],4.17[123]	4.245[125]
local magnetic moment on TM [μ_B]					
LSD KKR	4.07(4.27)	3.25(3.39)	2.20(2.33)	0.84(0.97)	0(0)
SIC-LSD KKR	4.60(4.60)	3.68(3.66)	2.69(2.68)	1.68(1.67)	0.76(0.76)
Expt.	4.79*,4.58*	3.32*	3.35*[127], 3.8*	1.77*,1.64*,1.90*	0.65*
SIC-LSD LMTO[120]	4.49	3.54	2.53	1.53	0.65
SIC-LSD LMTO[61]	4.64	3.55	2.59	1.49	0.64
bandgap [eV]					
LSD KKR	0.32	0	0	0	0
SIC-LSD KKR	3.29	3.40	2.76	3.44	1.79
Expt.	3.6-3.8*	2.4[128],2.5[129]	2.4*	4.3*,4.0*,4.3[130]	1.37*
SIC-LSD LMTO[120]	3.98	3.07	2.81	2.54	1.43
SIC-LSD LMTO[61]	3.57	3.25	2.51	2.66	1.00

* taken from ref. [120], for detailed references see references therein.
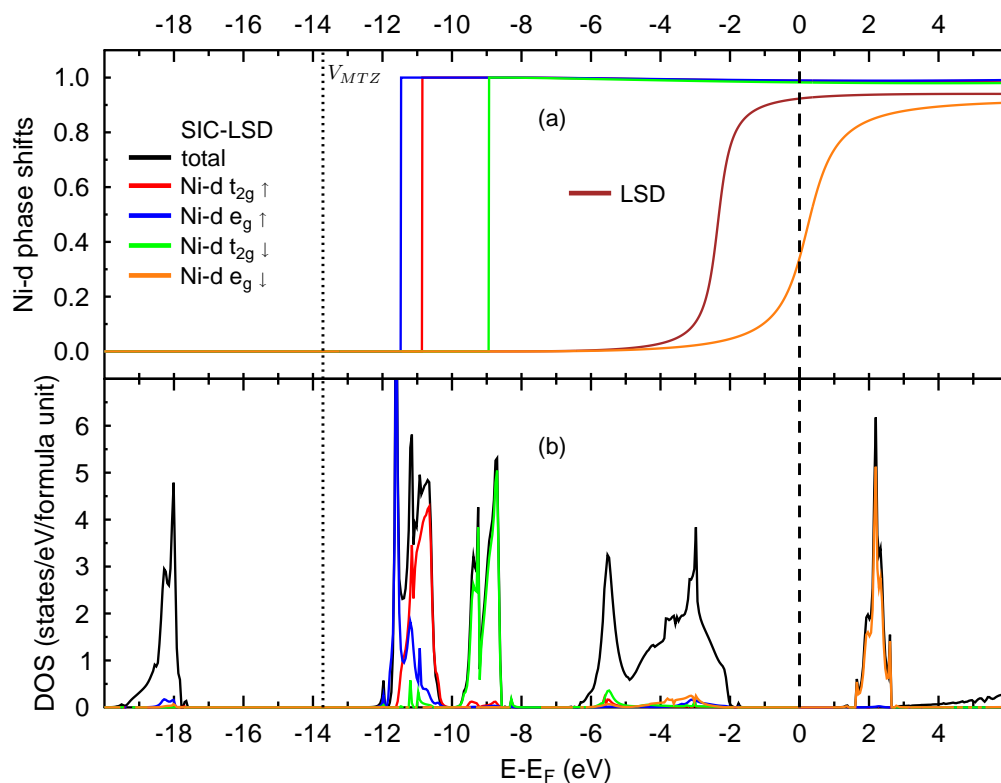
Figure 4.2. SIC-LSD KKR results for NiO: a) Ni-d phase shifts for LSDA and SIC-LSDA; b) DOS (black line) with the symmetry resolved Ni-d-fractions (colored lines). The color scheme is the same for all subfigures.
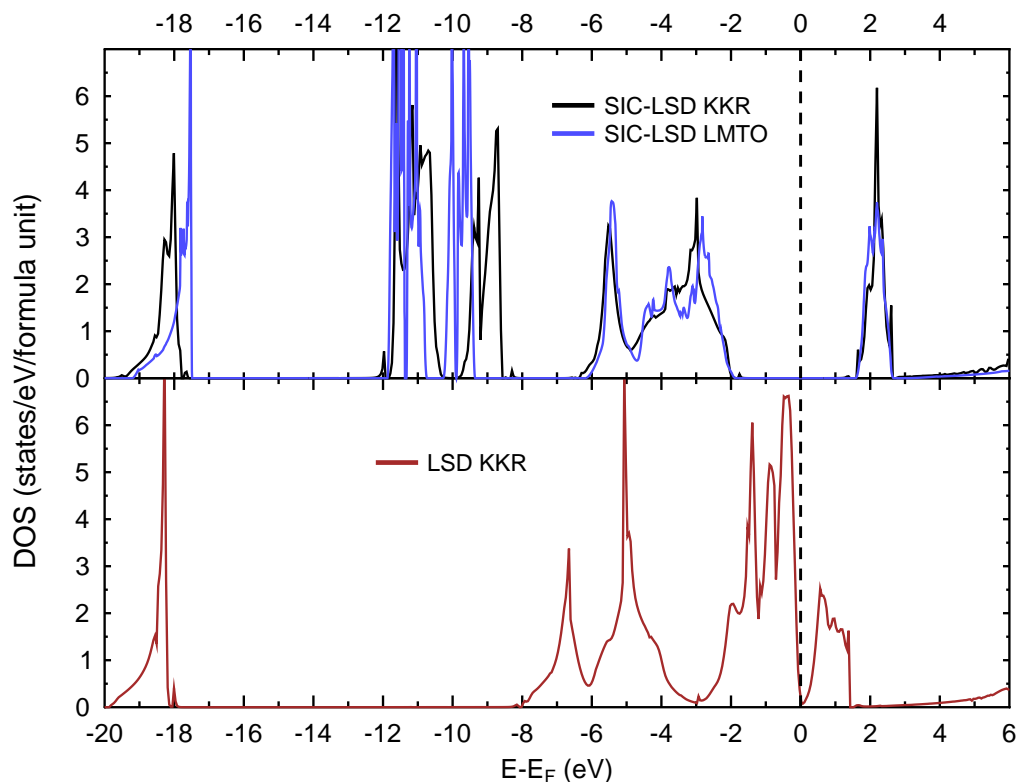
Figure 4.3. Density of states of NiO calculated with the SIC-LSD LMTO (blue line) and SIC-LSD KKR (black line) implementations compared to the LSD KKR calculation. The SIC results of the two different implementations are very similar.
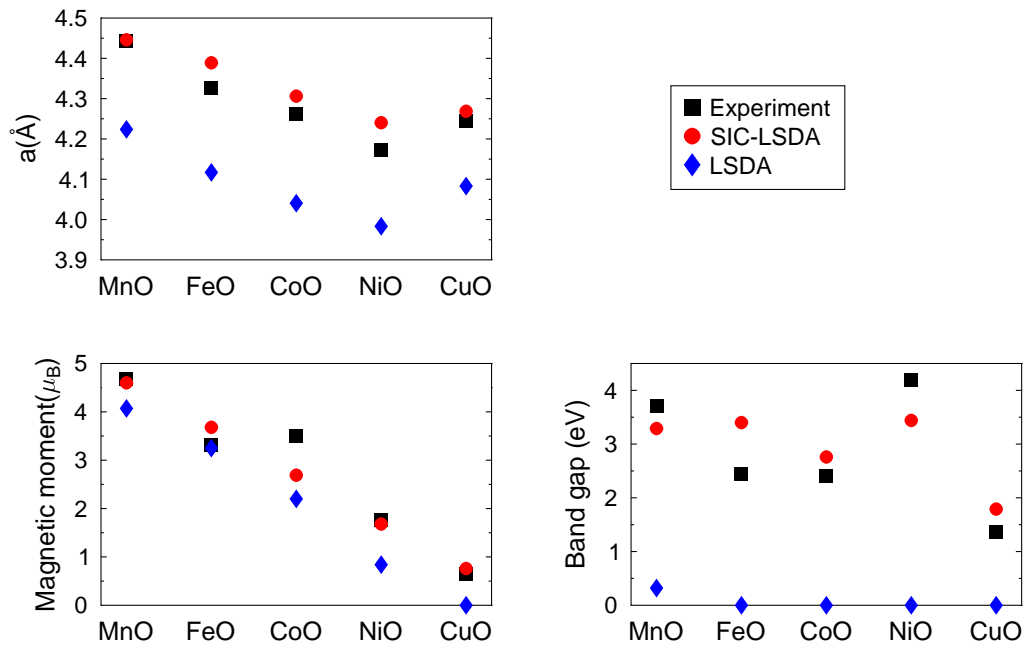
Figure 4.4. calculated equilibrium lattice constants, band gaps and local magnetic moment on TM for the TMO series (AF II structure). The band gaps and local moments are shown for the equilibrium lattice constant. The SIC-LSDA shows systematically better results. The local moment for CoO differs more comapred to the experimental value because spin orbit coupling is not included in the calculation.

5. Multiple scattering theory for surfaces and interfaces

One of the attractive features of the multiple-scattering theory is the separation of the structural information and potential dependent single-scattering parts. This provides flexibly to apply the KKR Green function method to systems with arbitrary geometry. To adapt a multiple scattering formalism to a particular geometry one has to modify adequately the structure constants and take into consideration appropriate boundary conditions. This flexibility makes the KKR Green function method very attractive for study of low dimensional systems. In particular, first-principles treatments of electronic structure of surface and interface have been provided within a number of Green function formalisms. One of the first multiple scattering approaches for surfaces was introduced by Pendry for the analysis of LEED[19] and photoemission spectra [20]. Later, this method was generalized for self-consistent calculations [27, 28]. With advance of the screening transformation for structure constants [52, 53] various implementations of the Green function method have been proposed to study the electronic structure of surfaces and interfaces [55, 64, 65]. The screened structure constants have a finite spatial extent and can be easily Fourier transformed corresponding to the symmetry of the problem. The screened KKR matrix for layered systems has a band form and can be efficiently inverted using a special technique with a computational effort of $\mathcal{O}(N)$. The short-range character of screened structure constants allows to take properly into account the semi-infinite nature of surfaces and interfaces. This makes the screened KKR method particularly attractive for spectroscopy and transport applications, for which any artifical confinement such as a supercell or a finite slab ruins the correct physical picture due to unphysical interaction between the boundaries.

Many modern experimental methods in surface physics, such as the scanning tunnel spectroscopy (STM) or photoemission, require an in-depth theoretical interpretation of their results. The importance of this fact motivated us to develop a KKR Green function method for semi-infinite systems. This method is a part of HUTSEPOT code and designed to study electronic, magnetic and transport properties of ordered and disordered surfaces and interface. Below presented are the main features of this formalism based on the References [53, 55, 64, 65, 131] and focus on an application of this approach to the photoemission spectroscopy.

5.1. Korringa-Kohn-Rostoker method for semi-infinite systems

As mentioned earlier, in the multiple scattering theory the calculation of the electronic structure is centered around the evaluation of the one-electron Green function (2.16), from which we may calculate the density of states, the charge density and, subsequently, the total energy. The key equation of the multiple scattering theory is the Dyson equation

$$\tau(E)^{ij} = \left\{ [t(E)^{-1} - g(E)]^{-1} \right\}_{ij} \tag{5.1}$$

for the scattering path operator $\tau(E)^{ij}$ connecting sites i and j. Here $t^i(E)$ is the potential dependent single-scattering t-matrix and $g(E)$ are real-space structure constants describing the free-particle propagator in the angular momentum representation. For systems with a two-dimensional (2D) lattice symmetry, such as surfaces or interfaces, it is advantageous to incorporate this symmetry into the formalism and perform the 2D Fourier transformations. The lattice-site vectors $\boldsymbol{R}_i$ can be decomposed as follows:

$$\boldsymbol{R}_i = \boldsymbol{R}_\parallel + S^{u\alpha} \tag{5.2}$$
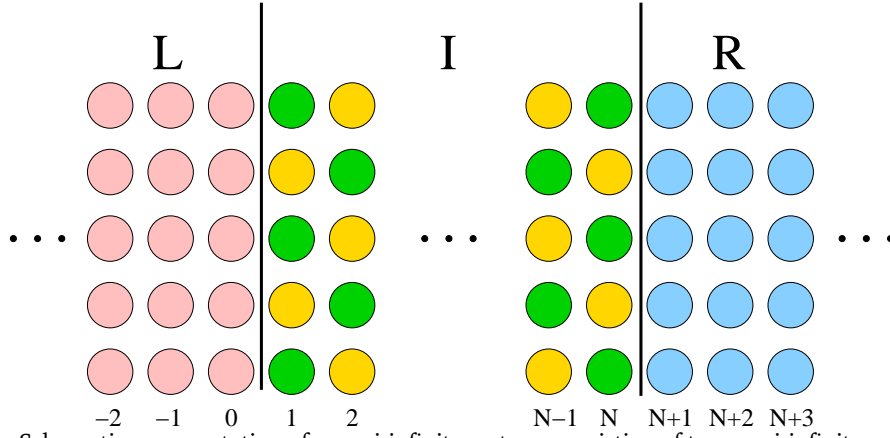
Figure 5.1. Schematic representation of a semi-infinite system, consisting of two semi-infinite regions L and R separated by a interface spacer I.

with u referring to the atomic position within a plane, and α labeling different planes. Employing the 2D Fourier transformed τ matrix,

$$\tau_{L,L'}^{u\alpha,v\beta}(\mathbf{k}_{\parallel}; \epsilon) = \sum_{\mathbf{R}_{\parallel}} e^{i\mathbf{k}_{\parallel}\mathbf{R}_{\parallel}} \, \tau_{L,L'}(\mathbf{R}_{\parallel}; \mathbf{S}^{u\alpha}, \mathbf{S}^{v\beta}; \epsilon) \,, \tag{5.3}$$

and the corresponding 2D Fourier transformation for structure constants $g(E)$, the Dyson equation (5.1) can be reformulated as

$$\tau^{u\alpha,u\beta}(\boldsymbol{k}_{\parallel}; E) = \left\{ [t(E)^{-1} - g(\boldsymbol{k}_{\parallel}; E)]^{-1} \right\}_{u\alpha,v\beta} \,, \tag{5.4}$$

where $\boldsymbol{k}_{\parallel}$ is a vector in the 2D Brillouin zone. This equation has to be solved for the appropriate boundary conditions. A semi-infinite system, corresponding to a surface or interface problem, is schematically presented in Fig.5.1. It consists of two semi-infinite subsystems, L (left) and R (right), which are separated by an interface I. The L subsystem can be referred as a host (bulk) system, where properties can be calculated using a 3D KKR method. The right side R may be another host material or vacuum. The interface region I is of main interest because this region is supposed to include all layers which are perturbed by the physical interface. It should be stressed that the left and right regions are semi-infinite and therefore, electrons in the whole system are not confined due to artificial boundaries such as a supercell or slab construction. This means that in order to solve the equation (5.4) one has to invert an infinite KKR matrix. The next serious problem is the evaluation of the Fourier transformed structure constants. A direct Fourier transformation of the real-space structure constants is not possible because of their slow convergence. This can be done with the Ewald technique [3], separating the sum over direct lattice vectors into two terms, both converging either in the direct or reciprocal spaces. The Ewald method for 2D structure constants was introduced by Kambe [132–134]. Evaluation of the Kambe structure constants is very time consuming and, moreover, the use of them makes it difficult to take into account the infinite number of layers in the equation (5.4). A more elegant way is to work with screened structure constants, which have short range spatial extent and can be easily Fourier transformed by direct summation over the lattice vectors as given in Eq. (5.3). Another important consequence of the short-range structure constants is the block-tridiagonal form of the KKR matrix, which can be represented as follows:

$$\tau(\boldsymbol{k}_{\parallel}; E)^{-1} \equiv \boldsymbol{M} = \begin{pmatrix} M_{LL} & M_{LI} & 0 \\ M_{IL} & M_{II} & M_{IR} \\ 0 & M_{RI} & M_{RR} \end{pmatrix} \,. \tag{5.5}$$

The scattering path operator $\tau_{II}(\boldsymbol{k}_{\parallel}; E)$, which refers to the interface–interface block, can be evaluated from the following equation:

$$\tau_{II}(\boldsymbol{k}_{\parallel}; E) = \left[M_{II} - M_{IL}(M_{LL})^{-1}M_{L,I} - M_{IR}(M_{RR})^{-1}M_{R,I} \right]^{-1} \,. \tag{5.6}$$

The main difficulty of the equation (5.6) lies in the last two terms, which include products of infinite matrices. This problem can be solved by introducing the so-called principal-layers partitioning [64, 131], where the structure constants are assumed nonzero only for nearest neighbor principal layers:

$$
\begin{aligned}
\left[M_{IL}(M_{LL})^{-1}M_{L,I}\right]^{PQ} &= M^{10}\Delta_L M^{01}\delta_{P,1}\delta_{Q,1} \\
\left[M_{IR}(M_{RR})^{-1}M_{R,I}\right]^{PQ} &= M^{01}\Delta_R M^{10}\delta_{P,N}\delta_{Q,N} \, .
\end{aligned}
\tag{5.7}
$$

Here P, Q are principal layer indices and the quantities Δ_L and Δ_R are related to the surface Green function in a tight-binding formalism [55, 64, 131]. The equations (5.7) can be effectively solved using the so-called decimation technique [135, 136], which is based on an iterative algorithm for treating infinite band matrices. Since the screened structure constants couple only a few neighboring layers, e.g., the nearest and next nearest layers, one can use a special algorithm for the matrix inversion [137] and, therefore, the number of computational steps needed to calculate the diagonal block matrices Eq. (5.6) scales linearly with the number of layers in the interface region. After solving the Dyson equation (5.4) the scattering path operator in this region can be evaluated by the following 2D Brillouin zone integral:

$$
\tau_{L,L'}(\mathbf{R}_\parallel; \mathbf{S}^{u\alpha}, \mathbf{S}^{v\beta}; \epsilon) = \frac{1}{\Omega}\int d\mathbf{k}_\parallel \tau_{L,L'}^{u\alpha, v\beta}(\mathbf{k}_\parallel; \epsilon)e^{-i\mathbf{k}_\parallel \mathbf{R}_\parallel} \, ,
\tag{5.8}
$$

where Ω is the volume of the two-dimensional Brillouin zone.

Once the layer-resolved scattering path operator (5.8) is determined, one can evaluate the one-electron Green function (2.16) and the corresponding density of states, charge and magnetization densities, the effective potentials and the total energy of the interface region. For the self-consistency it is very important to solve properly the Madelung problem taking into account appropriate boundary conditions. In our implementation we followed prescriptions suggested in [27, 28, 64] and extended the method to a full-potential approach.

After the self-consistent potentials of the interface region are established, the Green function may be used for many applications in surface and interface physics such as transport or angle-resolved photoemission.

Numerous successful applications of our method are presented in the appended publications.

In the references [P7,P8] we apply our method to study Fe/MgO/Fe(001) magnetic tunnel junction. This system is of particular interest because of a significant tunnel magnetoresistance effect, which was observed in this system. To study the impact of the crystal structure on Fe/MgO interface we calculate the electronic structure and the ballistic conductance within the Landauer-Büttiker theory. The conductance was estimated using omni2k [138] code on the bases of the self-consistent potentials obtained with using the HUTSEPOT program. Our calculations show large TMR values in the symmetric interface configuration, while asymmetric interface configuration decreases substantially the TMR effect. We explain this different behavior by interface resonance states induced by the FeO layer, which in the case of a symmetric magneto tunnel junction are present on both sides of the spacer. This leads to a strong enhancement of the conductance through these states.

In the next publication[P9], we focus on the Coulomb staircase in small Fe islands in Fe/MgO/Fe tunnel junction. The experimental analysis of the Coulomb staircase energetics reveals the expected linear behavior for electrostatic interaction. For ferromagnetic Fe islands, however, a significant offset of 1 eV was found, which is missing in the case of nonmagnetic Pd islands. This effect is explained by the spin dependence of the electronic transport across the MgO barrier in combination with a quasi-half-metallic density of states of the Fe islands, as corroborated by our first-principles electronic-structure calculations.

A study of surface relaxations of TiO_2 (110) (a combined study with HUTSEPOT and CRYS-TAL [139] codes) is presented in the publication [P10]. Successful structure determination entailed the development of adjustable parameter free self-consistent phase shifts, which provide

a more reliable description of the electron scattering than traditional approaches. The resulting optimized structure is remarkably consistent with that emerging from recent state of the art ab initio calculations. Additionally, the impact of soft surface vibrational modes on the structure determination has been investigated. It was found that the soft surface mode identified in this study has no significant bearing on the interpretation of the LEED-IV data, in contrast to suggestions in the literature.

A combined experimental and theoretical study of a giant spin splitting in the long-range surface alloy Bi/Ag(111) is presented in the reference [P11]. The long-range ordered surface alloy Bi/Ag(111) is found to exhibit a giant spin splitting of its surface electronic structure due to spin-orbit coupling, as is determined by angle-resolved photoelectron spectroscopy. First-principles electronic structure calculations (HUTSEPOT and omni2k) fully confirm the experimental findings. The effect is brought about by a strong in-plane gradient of the crystal potential in the surface layer, in interplay with the structural asymmetry due to the surface-potential barrier. As a result, the spin polarization of the surface states is considerably rotated out of the surface plane.

As a further example we present a formalism for calculating the angle-resolved photoemission based on our KKR Green function implementation.

5.2. Application: First-principles angle-resolved photoemission

In the photoemission process an electron absorbs a photon with the energy $\hbar\omega$ and is excited into a formally unoccupied state. If its energy is high enough to overcome the surface barrier, the electron can escape into the vacuum and eventually reach the detector. On its way through the solid the electron undergoes scattering processes with the lattice, the other electrons, and the phonons. The former will be treated by the multiple scattering theory, while the latter processes are many-particle processes, which are accounted for by the self-energy. The whole process can be described by non-equilibrium many-particle perturbation theory, as presented by Caroli *et al.* [140]. The lowest-order diagram of the expansion by Caroli *et al.* corresponds to the independent-particle picture of the photoemission [141]. Several efficient computational schemes, using a multiple-scattering description, have been developed within the independent particle approximation. In particular, the one-step model of the photoemission, developed by Pendry[20] using the layer KKR method has been successfully used in this field. This theory has been implemented in many flavors [21, 41, 142], but most of them are too complicated and restricted to special symmetries of the system. Here I describe a first-principles computational approach to the photoemission, based on multiple-scattering theory within the independent-particle approximation. The main advantage of this method is a unified treatment of the electronic structure and the photocurrent, using the Green function approach developed by Györffy and Stott [12] and the concept of the non-relativistic real-space theory for the photoemission by Durham [22].

Following the concept of the real-space photoemission formalism, the Green functions in the photocurrent formula can be expressed through the scattering matrix, τ, in the real-space representation. The real-space multiple-scattering theory offers a fertile field for investigations of systems with arbitrary arrangement of atoms. By making the appropriate Fourier transformation the formalism can easily be specialized to more symmetric systems, such as surfaces or multilayers.

In the present approach the self-consistent potentials for the photocurrent calculations have been obtained using the same formalism as for the photocurrent. We have implemented the KKR method both in the unscreened (Kambe [132–134]) as well as screened representation of the method [53, 64].

Here we will use the lowest order diagram of the expansion by Caroli [140] only, in which the

photocurrent at distance R is given by:

$$R^2 J^\lambda(\epsilon, \omega) = \frac{k}{4\pi} \frac{1}{(c\pi)^2} \int d^3r \int d^3r' \, \Psi_>(\mathbf{r};\mathbf{k}) \, \hat{O}^\lambda(\mathbf{r}) \, \mathrm{Im} G^r(\mathbf{r}, \mathbf{r}'; \epsilon) \times$$
$$\times \hat{O}^{\lambda\dagger}(\mathbf{r}') \, \Psi_>^*(\mathbf{r}';\mathbf{k}) \, \Theta(E_F - \epsilon) \, \Theta(\epsilon + \omega - V_{\mathrm{vac}}), \tag{5.9}$$

where $G^r(\mathbf{r}, \mathbf{r}'; \epsilon)$ is the retarded Kohn-Sham Green function of the system, E_F is the Fermi energy and V_{vac} is the vacuum potential.

$$\hat{O}^\lambda(\mathbf{r}) = \frac{1}{2c} \Big[\mathbf{A}^\lambda(\mathbf{r}) \hat{\mathbf{p}} - \hat{\mathbf{p}} \mathbf{A}^\lambda(\mathbf{r}) \Big] \tag{5.10}$$

describes the interaction with λ-polarised light, and $\Psi_>(\mathbf{r};\mathbf{k})$ is the so-called time-reversed LEED state, representing electrons leaving the solid into the vacuum. It is derived from the asymptotic form of the Green function and can be expressed via

$$\Psi_>(\mathbf{r},\mathbf{k}) = e^{i\mathbf{k}\mathbf{r}} + \int d^3r' e^{i\mathbf{k}\mathbf{r}'} v(\mathbf{r}') G^r(\mathbf{r}', \mathbf{r}; \tilde{\epsilon}), \tag{5.11}$$

where $\boldsymbol{k}$ is a wave vector of the emitted electron. We can now insert the KKR form of the Green function (2.16) into the LEED state (5.11) and the expression for the photocurrent (5.9), and obtain its scattering matrix representation. This can be decomposed into two contributions, according to the on-site and off-site terms in the scattering matrix representation of the Green function

$$R^2 J^\lambda(\epsilon, \omega) = M^\lambda(\epsilon, \omega) + I^\lambda(\epsilon, \omega). \tag{5.12}$$

For systems with a 2D lattice symmetry the off- and on-site contributions are respectively:

$$M^\lambda(\epsilon, \omega) = N \frac{4\pi k}{(c\pi)^2 \omega^2} \mathrm{Im} \sum_{\substack{u\alpha \\ v\beta}} \sum_{LL'} \sum_{L_2 L_2'} U_{L_2}^{u\alpha}(\mathbf{k}, \tilde{\epsilon}) e^{i\mathbf{q}\mathbf{S}^{u\alpha}} \times$$
$$F_{L_2 L}^{u\alpha\lambda(1)}(\epsilon, \omega) \tau_{LL'}^{u\alpha,v\beta}(\mathbf{k}_\parallel + \mathbf{q}_\parallel; \epsilon) F_{L_2' L'}^{v\beta\lambda(2)}(\epsilon, \omega) \times$$
$$e^{-i\mathbf{q}\mathbf{S}^{v\beta}} U_{L_2'}^{v\beta*}(\mathbf{k}; \tilde{\epsilon}) \tag{5.13}$$

$$I^\lambda(\epsilon, \omega) = N \frac{4\pi k}{(c\pi)^2 \omega^2} \mathrm{Im} \sum_{u\alpha} \sum_{LL'} U_L^{u\alpha}(\mathbf{k}, \tilde{\epsilon}) \, D_{LL'}^{u\alpha,\lambda}(\epsilon, \omega) \, U_{L'}^{u\alpha*}(\mathbf{k}; \tilde{\epsilon}), \tag{5.14}$$

where we have introduced the definitions

$$U_L^{u\alpha}(\mathbf{k}, \tilde{\epsilon}) = \sum_{L_1} i^{l_1} Y_{L_1}^*(\hat{\mathbf{k}}) \sum_{v\beta} e^{i\mathbf{k}\mathbf{S}^{v\beta}} \tau_{L_1 L}^{v\beta,u\alpha}(\mathbf{k}_\parallel; \tilde{\epsilon}) \tag{5.15}$$

$$F_{LL'}^{u\alpha\lambda(1)}(\epsilon, \omega) = \int d^3r_{u\alpha} Z_L^{u\alpha}(\mathbf{r}_{u\alpha}, \tilde{\epsilon}) \, \tilde{\chi}_{u\alpha}^\lambda(\mathbf{r}_{u\alpha}) \, \bar{Z}_{L'}^{u\alpha}(\mathbf{r}_{u\alpha}; \epsilon) \tag{5.16}$$

$$F_{LL'}^{u\alpha\lambda(2)}(\epsilon, \omega) = \int d^3r_{u\alpha} Z_L^{u\alpha*}(\mathbf{r}_{u\alpha}, \tilde{\epsilon}) \, \tilde{\chi}_{u\alpha}^\lambda(\mathbf{r}_{u\alpha}) \, Z_{L'}^{u\alpha}(\mathbf{r}_{u\alpha}; \epsilon) \tag{5.17}$$

$$D_{L_2 L_2'}^{u\alpha\lambda}(\epsilon, \omega) = \sum_L \int d^3r_{u\alpha} \int d^3r_i' Z_{L_2}^{u\alpha}(\mathbf{r}_{u\alpha}; \tilde{\epsilon}) \, \tilde{\chi}_{u\alpha}^\lambda(\mathbf{r}_{u\alpha}) \bar{Z}_L^{u\alpha}(\mathbf{r}_<; \epsilon) \times$$
$$J_L^{u\alpha}(\mathbf{r}_>; \epsilon) \, \tilde{\chi}_{u\alpha}^\lambda(\mathbf{r}_{u\alpha}') \, Z_{L_2'}^{u\alpha*}(\mathbf{r}_{u\alpha}'; \tilde{\epsilon}). \tag{5.18}$$

To demonstrate the method described above, we choose the well studied copper surface, and, in particular, we investigate the features of the *sp*-band, seen on the (100) surface, and the surface-state on (111) surface. The potentials for the respective calculations were determined

self-consistently using the layer-KKR method, presented in Sec. 5.1. The potentials for the interface system, consisting of 10 Cu layers and three layers of empty spheres (to represent the vacuum) have been updated self-consistently. In what follows we refer to the surface layer of this system as S and to the subsequent layers below the surface as $S_{-1}, S_{-2}, \ldots$. The empty sphere layers are denoted by $S_1, S_2, \ldots$. The boundary conditions for both infinite half spaces are such that the Cu bulk potential has been used for all layers from S_{-11} to $S_{-\infty}$ and the empty sphere potential of the outermost vacuum layer, S_3, has been repeated for S_4 to S_∞. In the calculations these infinite half spaces have been treated with the decimation technique [137]. Therefore the potentials, used for the (100) and (111) surfaces differ from each other. As a demonstration of this, we show in Table 5.1 the evaluated work functions, which were then used in the photoemission calculations.

	present work	Turek	Skriver	Experiment
Cu (100)	5.25	5.21	5.26	4.59
Cu (111)	5.46	5.16	5.30	4.94

Table 5.1. Workfunctions Φ in eV obtained in this method compared with other theoretical and with experimental values, both taken from references [143, 144]
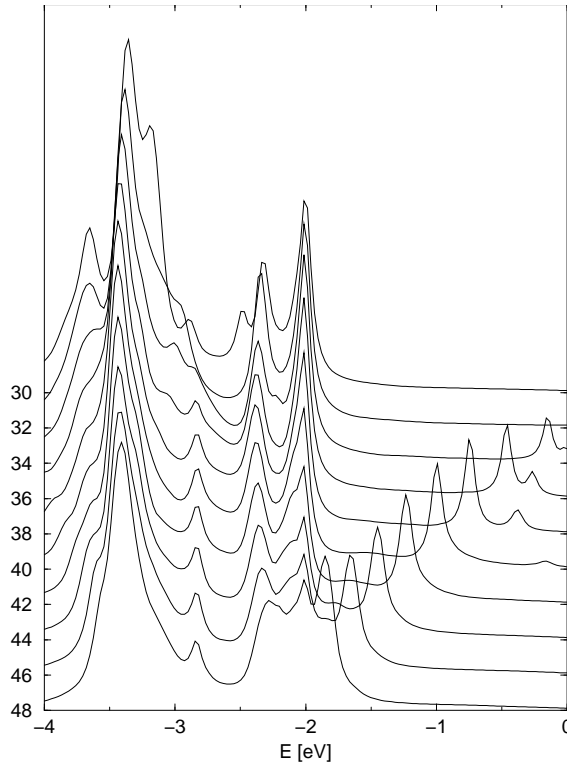
Figure 5.2. Photocurrent of Cu (100) at 21.2 eV in the $\Gamma XULK$ -plane. The calculations were performed with hole linewidth of 0.05 eV and an electron linewidth of 1.3 eV. 11 Cu layers and 10 vacuum layers were contributing to the photocurrent, and the KKR matrix was inverted for a system of 16 Cu and 15 empty sphere layers.

Figure 5.2 shows a series of photoemission spectra for different emission angles. What can be clearly observed here is the d-band feature at binding energies between -2 and -4 eV, and the *sp*-band reaching up to the Fermi-level. These results are in good agreement with the experimental spectra and previous calculations [145]. As another example of our photoemission approach, we study the surface state on the (111) surface of copper. The experimental [146] and calculated results for the total photocurrent at 21.2 eV photon energy are shown in Figs. 5.3 and 5.4. The surface state is clearly observed at -0.9 eV in the calculations. Since it is only visible with p-polarised light, one can already conclude that the state has Λ_3 symmetry. The position of the

surface state in the theory is about 0.4 eV lower than in the experiment. This error is related to the LSD approximation, which is known to fail on correct description of surface states in nobel metals.

Thus, we demonstrated, that our method can reproduce experimental spectra. For an interpretation of photoemission experiments we combine a photocurrent study with investigating the Bloch spectral function calculated with the same method. This combination provides insight into the nature of the photoemission peaks. Another strong point of this method is that the self-consistent calculation and the calculation of the spectral functions and the photocurrent are based on the same method and are preformed with the same code. More details of our approach can be found in the related papers [26, 82].

An example of a photoemission study in the Ag/V (001) multilayer system is presented in the attachment [P12]. Quantum-well states in the Ag films show the typical dispersion with film thickness, but their spectral densities differ significantly from those of model systems. Ab initio calculations for several systems (bulk, surfaces, interfaces, and thin films) reveal as origins band-structure effects and hybridization between Ag and V states. Quantization effects show up as intensity oscillations in the constant-initial-state mode of photoelectron spectroscopy.
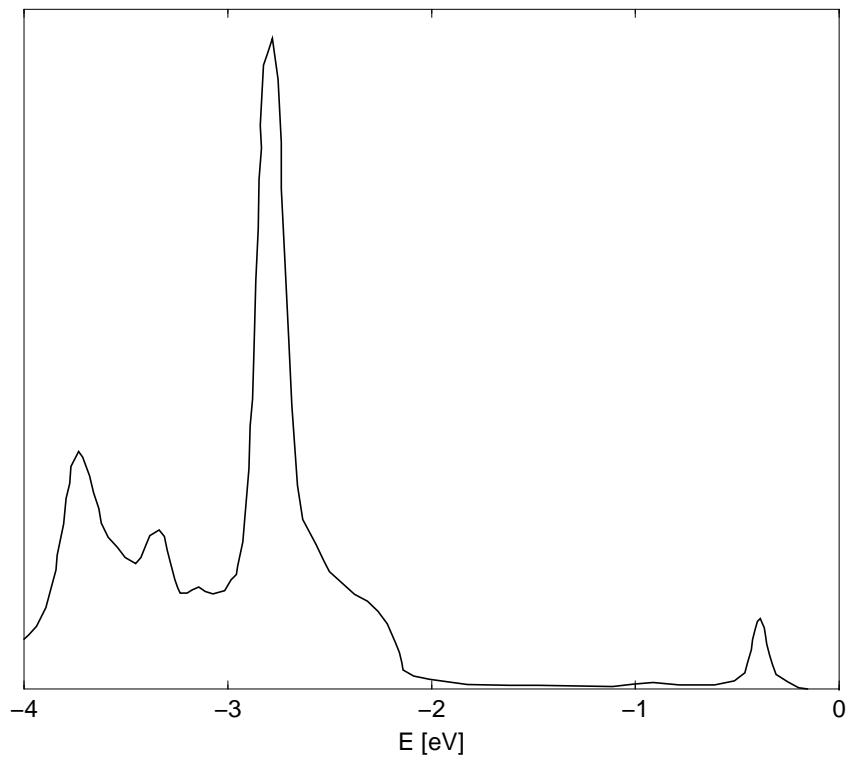
Figure 5.3. Experimental photocurrent of Cu (111) at 21.2 eV normal emission.
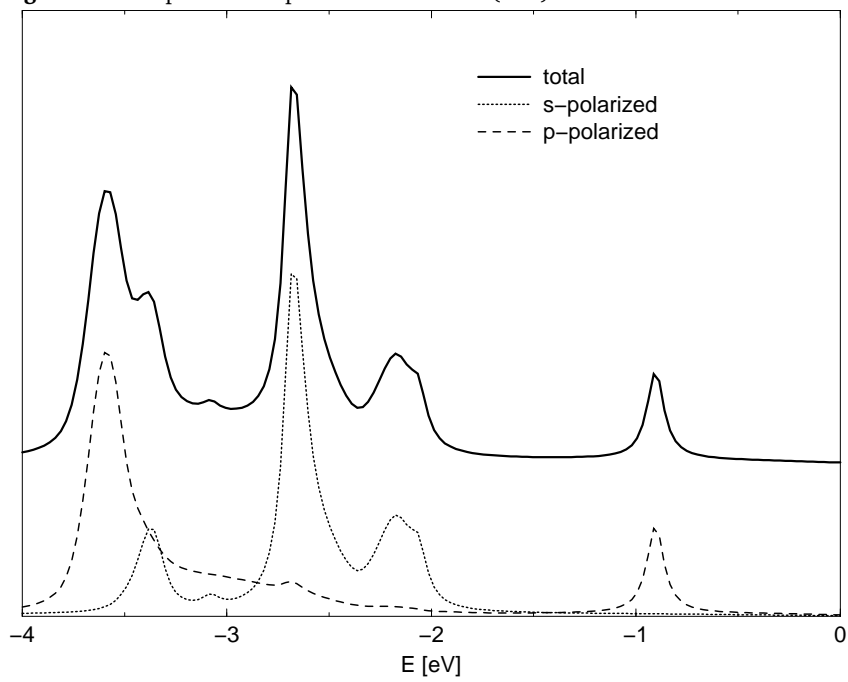
Figure 5.4. Polarisation resolved photocurrents of Cu (111) at 21.2 eV normal emission.

6. Conclusion and outlook

In this thesis there are presented some novel aspects of the multiple-scattering theory, designed for first-principles electronic structure calculations of complex materials.

One of the important new features is the multiple scattering implementation of the self-interaction correction (SIC) approach, which enables realistic electronic structure calculations of systems with localized electrons. This formalism is generalized to the coherent potential approximation (CPA), extending the application area to random alloys. A combination of the SIC approach and the CPA allows for descriptions of static charge and spin fluctuations in terms of a pseudoalloy, composed of the delocalized and localized states with different orientations of the local magnetic moment. The generalization of this formalism to finite temperatures opens for the SIC approach new application fields such as phase transitions or thermal fluctuations in correlated materials. The functionality of this method was demonstrated on the application to the Ce α-γ transition, on the study of magnetic and structural properties of rare earth elements and transition metal oxides.

Another important innovation of this thesis is the implementation of the self-consistent non-local CPA (NLCPA) approach, which takes into account charge correlations around the CPA average and chemical short range order. Several improvements for the basic algorithm and a symmetrization of the fundamental coarse-graining procedure were elaborated to optimize the computational performance of the NLCPA method. This formalism was extended to the relativistic treatment of magnetically ordered systems. The power of the NLCPA scheme was demonstrated by applications to $Cu_{50}Zn_{50}$, $Cu_{60}Pd_{40}$, $Cu_{77}Ni_{23}$ and $Fe_{50}Pt_{50}$ random alloys.

Many conceptual improvements of the KKR Green function formalism were suggested in this work. The most important of them is the implementation of the Lloyd formula, which significantly accelerates the angular momentum convergence of the Green function and minimizes errors due to the truncation of the angular momentum summations. A combination of the Lloyd correction with the full charge density or full potential approaches enables very accurate total energy calculations which are comparable to well established all-electron full-potential variational methods.

All these new features are implemented within the multifunctional KKR Green function code HUT-SEPOT, which is designed to study structural, electronic, magnetic, transport and spectroscopic properties of ordered and disordered systems with arbitrary symmetries. The versatility of the method is illustrated in numerous applications presented in the appended publications.

The presented formalism has a flexible design and is being constantly developed and improved. The great potential of this method is the straightforward determination of the one-electron Green function, which is an important constituent of many applications. Presently, a GW approximation for the description of excited state properties and a non-adiabatic spin dynamic approach are under construction. Further development of this method can be proposed to a first-principles dynamical mean field theory (DMFT). This can be achieved by the inclusion of dynamical valence and spin fluctuations in the framework of the SIC-LSD formalism. In this respect, short-range correlations of spin and charge fluctuations in many-electron systems can be described with the NLCPA approach.

Bibliography

[1] J. W. Rayleigh. Philosophical Magazine **23** (1892) 481.

[2] N. Kasterin. Vers. Akad. van Wetensch. Amsterdam **6** (1897) 460.

[3] P. P. Ewald. Ann. Phys. **49** (1916) 1.

[4] J. Korringa. Physica **13** (1947) 392.

[5] W. Kohn. Phys. Rev. **87** (1952) 847.

[6] W. Kohn, N. Rostoker. Phys. Rev. **94** (1954) 1111.

[7] J. C. Slater. Phys. Rev. **51** (1937) 840.

[8] F. S. Ham, B. Segall. Phys. Rev. **124** (1961) 1786.

[9] O. K. Andersen. Phys. Rev. B **12** (1975) 3060.

[10] G. J. Morgan. Proc. Phys. Soc. London **89** (1966) 365.

[11] J. L. Beeby. Proc. Roy. Soc. London **Ser. A302** (1967) 113.

[12] B. L. Gyorffy, M. J. Stott. In D. J. Fabian, L. M. da Watson (Hrsg.), *Band Structure Spectroscopy of Metals and Alloys*, S. 385 (Academic, New York, 1972).

[13] P. Soven. Phys. Rev. **156** (1967) 809.

[14] B. L. Gyorffy. Phys. Rev. B **5** (1972) 2382.

[15] G. M. Stocks, W. M. Temmerman, B. L. Gyorffy. Phys. Rev. Lett. **41** (1978) 339.

[16] A. Bansil. Phys. Rev. Lett. **41** (1978) 1670.

[17] R. Zeller, P. H. Dederichs. Phys. Rev. Lett. **42** (1979) 1713.

[18] W. M. Temmerman. J. Phys. F: Met. Phys. **12** (1982) L25.

[19] J. B. Pendry. *Low Energy Electron Diffraction* (Academic Press, London, 1974).

[20] J. B. Pendry. Surf. Sci. **57** (1976) 679.

[21] J. F. L. Hopkinson, J. B. Pendry, D. J. Titterington. Comp. Phys. Commun. **19** (1980) 69.

[22] P. J. Durham. J. Phys. F: Met. Phys. **11** (1981) 2475.

[23] G. Thörner, G. Borstel. phys. stat. sol. (b) **126** (1984) 617.

[24] S. V. Halilov, E. Tamura, H. Gollisch, R. Feder, B. Kessler, N. Müller, U. Heinzmann. J. Phys.: Condens. Matt. **5** (1993) 3851.

[25] J. Henk, S. V. Halilov, T. Scheunemann, R. Feder. Phys. Rev. B **50** (1994) 8130.

[26] M. Lüders, A. Ernst, W. M. Temmerman, Z. Szotek, P. J. Durham. J. Phys.: Condens. Matt. **13** (2001) 8587.

[27] J. M. MacLaren, S. Crampin, D. D. Vvedensky, J. B. Pendry. Phys. Rev. B **40** (1989) 12 164.

[28] J. M. MacLaren, S. Crampin, D. D. Vvedensky. Phys. Rev. B **40** (1989) 12 176.

[29] L. Baumgarten, C. M. Schneider, H. Petersen, F. Schäfers, J. Kirschner. Phys. Rev. Lett. **65** (1990) 492.

[30] S. Kaprzyk, A. Bansil. Phys. Rev. B **42** (1990) 7358.

[31] P. Strange, P. J. Durham, B. L. Gyorffy. Phys. Rev. Lett. **67** (1991) 3590.

[32] H. Ebert, G. Schütz (Hrsg.). *Magnetic Dichroism and Spin Polarization in Angle-Resolved Photoemission*. Number 466 in Lecture Notes in Physics (Springer, Berlin, 1996).

[33] T. Huhne, H. Ebert. Phys. Rev. B **60** (1999) 12 982.

[34] A. Vernes, L. Szunyogh, P. Weinberger. Phys. Rev. B **65** (2002) 144448.

[35] G. Hörmandinger, P. Weinberger, P. Marksteiner, J. Redinger. Phys. Rev. B **38** (1988) 1040.

[36] L. Szunyogh, P. Weinberger, J. Redinger. Phys. Rev. B **46** (1992) 2015.

[37] J. Minár, V. Popescu, H. Ebert. Phys. Rev. B **62** (2000) 10 051.

[38] R. Feder, H. Gollisch, D. Meinert, T. Scheunemann, O. M. Artamonov, S. N. Samarin, J. Kirschner. Phys. Rev. B **58** (1998) 16 418.

[39] N. Fominykh, J. Henk, J. Berakdar, P. Bruno, H. Gollisch, R. Feder. Sol. State Commun. **113** (2000) 665.

[40] R. Feder, F. Rosicky, B. Ackermann. Z. Phys. B **52** (1983) 31.

[41] B. Ackermann, R. Feder, E. Tamura. J. Phys. F: Met. Phys. **14** (1984) L173.

[42] P. Strange, J. Staunton, B. L. Gyorffy. J. Phys. C: Solid State Phys. **17** (1984) 3355.

[43] B. L. Gyorffy, A. J. Pindor, J. Staunton, G. M. Stocks, H. Winter. J. Phys. F: Met. Phys. **15**

(1985) 1337.

[44] J. Staunton, B. L. Gyorffy, A. J. Pindor, G. M. Stocks, H. Winter. J. Phys. F: Met. Phys. **15** (1985) 1387.

[45] J. Staunton, B. L. Gyorffy, G. M. Stocks, J. Wadsworth. J. Phys. F: Met. Phys. **16** (1986) 1761.

[46] E. Stenzel, H. Winter. J. Phys. F: Met. Phys. **15** (1985) 1571.

[47] A. I. Liechtenstein, M. I. Katsnelson, V. P. Antropov, V. A. Gubanov. J. Magn. Magn. Mat. **67** (1987) 65.

[48] L. M. Sandratskii. Phys. Status Solidi B **135** (1986) 167.

[49] P. Strange, H. Ebert, J. B. Staunton, B. L. Gyorffy. J. Phys.: Condens. Matt. **1** (1989) 3947.

[50] L. Szunyogh, B. Újfalussy, P. Weinberger. Phys. Rev. B **51** (1995) 9552.

[51] S. S. A. Razee, J. B. Staunton, F. J. Pinski. Phys. Rev. B **56** (1997) 8082.

[52] O. K. Andersen, O. Jepsen. Phys. Rev. Lett. **53** (1984) 2571.

[53] R. Zeller, P. H. Dederichs, B. Újfalussy, L. Szunyogh, P. Weinberger. Phys. Rev. B **52** (1995) 8807.

[54] L. Szunyogh, B. Újfalussy, P. Weinberger, J. Kollár. J. Phys.: Condens. Matt. **6** (1994) 3301.

[55] K. Wildberger, R. Zeller, P. H. Dederichs. Phys. Rev. B **55** (1997) 10 074.

[56] J. Opitz, P. Zahn, I. Mertig. Phys. Rev. B **15** (2003) 245417.

[57] Y. Wang, G. M. Stocks, W. A. Shelton, D. M. C. Nicholson, Z. Szotek, W. M. Temmerman. Phys. Rev. Lett. **75** (1995) 2867.

[58] W. H. Butler. Phys. Rev. B **41** (1990) 2684.

[59] J. P. Perdew, A. Zunger. Phys. Rev. B **23** (1981) 5048.

[60] A. Svane, O. Gunnarsson. Phys. Rev. Lett. **65** (1990) 1148.

[61] Z. Szotek, W. M. Temmerman, H. Winter. Phys. Rev. B **47** (1993) 4029.

[62] J. S. Faulkner, G. M. Stocks. Phys. Rev. B **21** (1980) 3222.

[63] P. Weinberger. *Electron Scattering Theory of Ordered and Disordered Matter* (Clarendon Press, Oxford, 1990).

[64] L. Szunyogh, B. Újfalussy, P. Weinberger, J. Kollár. Phys. Rev. B **49** (1994) 2721.

[65] C. Uiberacker, L. Szunyogh, B. Újfalussy, P. Weinberger, A. Ernst, P. H. Dederichs. Phil. Mag. B **78** (1998) 423.

[66] L. Petit, S. V. Beiden, W. M. Temmerman, Z. Szotek, G. M. Stocks, G. G. A. J. Phys.: Condens. Matt. **12** (2000) 8439.

[67] B. L. Györffy, G. M. Stocks. In P. Phariseau (Hrsg.), *Electrons in Finite and Infinite Structures* (Plenum Press, New York, 1977).

[68] M. Jarrell, H. R. Krishnamurthy. Phys. Rev. B **63** (2001) 125102.

[69] D. A. Rowlands, J. B. Staunton, B. L. Györffy. Phys. Rev. B **67** (2003) 115109.

[70] D. A. Rowlands. *The KKR-NLCPA: a new method for describing the electronic structure of disordered metallic systems*. Dissertation, University of Warwick (2004).

[71] D. A. Rowlands, J. B. Staunton, B. L. Györffy, E. Bruno, B. Ginatempo. Phys. Rev. B **72** (2005) 045101.

[72] A. Gonis. *Green Functions for Ordered and Disordered Systems*, Bd. 4 der *Studies in Mathematical Physics* (North-Holland, Amsterdam, 1992).

[73] P. Lloyd. Proc. Phys. Soc. London **90** (1967) 207.

[74] P. Lloyd, P. V. Smith. Adv. Phys. **21** (1972) 69.

[75] B. Drittler, M. Weinert, R. Zeller, P. H. Dederichs. Phys. Rev. B **39** (1989) 930.

[76] H. Akai, P. H. Dederichs. Phys. Rev. B **47** (1993) 8739.

[77] K. Gunkel. *Gesamtenergieberechnung mit Lloydscher Formel für den Idealkristall*. Dissertation, Rheinisch-Westfälische Technische Hochschule Aachen (1993).

[78] A. F. Tatarchenko, N. I. Kulikov. Phys. Rev. B **50** (1994) 8266.

[79] A. Lodder, J. P. Dekker. Phys. Rev. B **49** (1994) 10 206.

[80] A. Lodder, P. J. Braspenning. Phys. Rev. B **49** (1994) 10 215.

[81] R. Zeller. J. Phys.: Condens. Matter **16** (2004) 6453.

[82] A. Ernst, W. M. Temmerman, Z. Szotek, M. Woods, P. J. Durham. Phil. Mag. B **78** (1998) 503.

[83] J. Henk, A. Ernst, K. K. Saha, P. Bruno. J. Phys.: Condens. Matter **18** (2006) 2601.

[84] W. H. Butler, X.-G. Zhang. Phys. Rev. B **44** (1991) 969.

[85] N. Y. Maghadam, G. M. Stocks, X.-G. Zhang, D. M. C. Nicholson, W. A. Shelton, Y. Wang,

J. S. Faulkner. J. Phys.: Condens. Matt. **13** (2001) 3073.

[86] D. A. Rowlands, A. Ernst, J. B. Staunton, B. L. Györffy. Phys. Rev. B **73** (2006) 165122.

[87] F. Maca, J. Masek. Phys. Rev. B **65** (2002) 235209.

[88] J. Masek, J. Kudrnovský, F. Maca. Phys. Rev. B **67** (2003) 153203.

[89] X.-G. Zhang, D. M. C. Nicholson. Phys. Rev. B **60** (1999) 4551.

[90] S. Limpijumnong, W. R. L. Lambrecht. Phys. Rev. Lett. **86** (2001) 91.

[91] S. Limpijumnong, W. R. L. Lambrecht. Phys. Rev. B **63** (2001) 104103.

[92] S. Limpijumnong, S. Jungthawan. Phys. Rev. B **70** (2004) 054104.

[93] H. Sowa. Acta Cryst. A **57** (2001) 176.

[94] J. E. Jaffe, J. A. Snyder, Z. Lin, A. V. Hess. Phys. Rev. B **62** (2000) 1660.

[95] Y.-S. Kim, E.-C. Lee, K. J. Chang. J. Korean Phys. Soc. **39** (2001) 92.

[96] A. Seko, F. Oba, A. Kuwabara, I. Tanaka. Phys. Rev. B **72** (2005) 024107.

[97] S. Desgreniers. Phys. Rev. B **58** (1998) 14102.

[98] H. Karzel, W. Potzel, M. Köfferlein, W. Schissl, M. Steiner, U. Hiller, G. M. Kalvius, D. W. Mitchell, T. P. Das, P. Blaha, K. Schwarz, M. P. Pasternak. Phys. Rev. B **53** (1996) 11425.

[99] A. N. Baranov, V. S. Stepanyuk, W. Hergert, A. A. Katsnelson, A. Settels, R. Zeller, P. H. Dederichs. Phys. Rev. B **66** (2002) 155117.

[100] R. W. G. Wyckoff. *Crystal Structures*, Bd. 1 (Interscience Publishers, New York, 1963), 2nd edition.

[101] M. J. L. Sangster, A. M. Stoneham. Philos. Mag. B **43** (1981) 597.

[102] M. J. L. Sangster, G. Peckham, D. H. Saunderson. J. Phys. C: Solid State Phys. **3** (1970) 1026.

[103] A. J. Cohen, R. G. Gordon. Phys. Rev. B **14** (1981) 4593.

[104] M. Sanati, G. L. W. Hart, A. Zunger. Phys. Rev. B **68** (2003) 155210.

[105] A. Ohtomo, M. Kawasaki, T. Koida, K. Masubuchi, H. Koinuma, Y. Sakurai, Y. Yoshida, T. Yasuda, Y. Segawa. App. Phys. Lett. **72** (1998) 2466.

[106] J. P. Perdew, A. Zunger. Phys. Rev. B **23** (1981) 5048.

[107] R. A. Heaton, J. G. Harrison, C. C. Lin. Phys. Rev. B **28** (1983) 5992.

[108] P. Strange, A. Svane, W. M. Temmerman, Z. Szotek, H. Winter. Nature **399** (1999) 756.

[109] A. Svane, W. M. Temmerman, Z. Szotek, L. Petit, P. Strange, H. Winter. Phys. Rev. B **62** (2000) 13394.

[110] W. M. Temmerman, H. Winter, Z. Szotek, A. Svane. Phys. Rev. Lett. **86** (2001) 2435.

[111] L. Petit, A. Svane, Z. Szotek, W. M. Temmerman. Science **301** (2003) 498 .

[112] Z. Szotek, W. M. Temmerman, A. Svane, L. Petit, G. M. Stocks, H. Winter. Phys. Rev. B **68** (2003) 054415.

[113] R. Tyer, W. M. Temmerman, Z. Szotek, G. Banach, A. Svane, L. Petit, G. A. Gehring. Europhys. Lett. **65** (2004) 519.

[114] G. Banach, W. M. Temmerman. Physical Review B (Condensed Matter and Materials Physics) **69** (2004) 054427.

[115] W. M. Temmerman, A. Svane, Z. Szotek, H. Winter. In J. F. Dobson, G. Vignale, M. P. Das (Hrsg.), *Electronic Density Functional Theory: Recent Progress and New Directions*, S. 327 (Plenum Press, New York, 1998).

[116] R. A. Heaton, J. G. Harrison, C. C. Lin. Phys. Rev. B **28** (1983) 5992.

[117] W. Kohn, L. J. Sham. Phys. Rev. **140** (1965) A1133.

[118] V. I. Anisimov, F. Aryasetiawan, A. I. Lichtenstein. J. Phys.: Condens. Matt. **9** (1997) 767.

[119] A. Georges, G. Kotliar, W. Krauth, M. Rozenberg. Reviews of Modern Physics **68** (1996) 13.

[120] A. Svane, O. Gunnarsson. Phys. Rev. Lett. **65** (1990) 1148.

[121] D. Ködderitzsch, W. Hergert, W. M. Temmerman, Z. Szotek, A. Ernst, H. Winter. Phys. Rev. B **66** (2002) 064434.

[122] S. Sasaki, K. Fujino, Y. Takéuchi, R. Sadanaga. Acta Crystallographica Section A **36** (1980) 904.

[123] G. I. Landoldt-Börnstein, New Series. *Numerical Data and Functional Relations in Science and Technology*, Bd. 27g, Various Other Oxides (Springer Verlag, 1992).

[124] H. Fjellvåga, F. Grønvolda, S. Stølen, B. Hauback. Journal of Solid State Chemistry **124** (1996) 52.

[125] N. G. Schmahl, G. F. Eikerling. Zeitschrift für Physikalische Chemie (Muenchen, Germany)

62 (1968) 268.

[126] N. G. Schmahl, J. Barthel, G. F. Eikerling. Zeitschrift für anorganische und allgemeine Chemie **332** (1964) 230 .

[127] D. C. Khan, R. A. Erickson. Phys. Rev. B **1** (1970) 2243.

[128] D. A. H.K. Bowen, B. Auker. Journal of Solid State Chemistry **12** (1975) 355.

[129] B.-s. Kim, S. Hong, D. W. Lynch. Phys. Rev. B **41** (1990) 12227.

[130] G. A. Sawatzky, J. W. Allen. Phys. Rev. Lett. **53** (1984) 2339.

[131] B. Wenzien, J. Kudrnovský, V. Drchal, M. Šob. J. Phys.: Condens. Matt. **1** (1989) 9893.

[132] K. Kambe. Z. Naturf. **22a** (1967) 422.

[133] K. Kambe. Z. Naturf. **22a** (1967) 322.

[134] K. Kambe. Z. Naturf. **22a** (1967) 1280.

[135] M. P. Lopéz Sancho, J. M. L. Sancho, J. Rubio. J. Phys. F: Met. Phys. **15** (1985) 851.

[136] M. P. L. Sancho, L. Chiro, M. C. M. noz. Europhys. Lett. **40** (1997) 679.

[137] E. M. Godfrin. J. Phys.: Condens. Matt. **3** (1991) 7843.

[138] J. Henk, T. Scheunemann, S. V. Halilov, E. Tamura, R. Feder. OMNI2K—Fully relativistic electron spectroscopy calculations (2005). The computer code is available from the authors.

[139] V. R. Saunders, R. Dovesi, C. Roetti, R. Orlando, C. M. Zicovich-Wilson, N. M. Harrison, K. Doll, B. Civalleri, I. Bush, P. D'Arco, L. M. Crystal 2003: User's manual (university of turin, turin, 2003) (2003).

[140] C. Caroli, D. Lederer-Rozenblatt, B. Roulet, D. Saint-James. Phys. Rev. B **8** (1973) 4552.

[141] P. J. Feibelman, D. E. Eastman. Phys. Rev. B **10** (1974) 4932.

[142] J. Braun, M. Donath. J. Phys.: Condens. Matt. **16** (2004) S2539.

[143] H. L. Skriver, N. M. Rosengaard. Phys. Rev. B **45** (1992) 9410.

[144] I. Turek, V. Drchal, J. Kurdnovský, M. Sob, P. Weinberger. *Electronic Structure of Disordered Alloys, Surfaces and Interfaces* (Kluwer Academic Publishers,Boston-Dordrecht-London, 1997).

[145] P. J. Durham, N. Kar. Surf. Sci **111** (1981) L648.

[146] M. Fluchtmann, S. Bei der Kellen, J. Braun, G. Borstel. Surf. Sci **402-404** (1998) 663.

Acknowledgment

Eidesstattliche Erklärung

Hiermit erkläre ich, dass ich die Habilitationsschrift selbstständig und ohne fremde Hilfe verfasst und andere als die angegebenen Quellen und Hilfsmittel nicht benutzt und die den benutzten Werken wörtlich oder inhaltlich entnommenen Stellen als solche kenntlich gemacht habe.

Halle (Saale), den May 10, 2007

Dr. Arthur Ernst

Lebenslauf

Dr. Arthur Ernst

Anschrift

	Privat	**Beruflich**
Adresse:	Breitestraße 23	MPI für Mikrostrukturphysik
	D-06108 Halle	Weinberg 2
		D-06120 Halle (Saale)
Email:		aernst@mpi-halle.de
Telefon:	+49 (0)345 2 90 82 80	+49 (0)345 5582–666
Fax:		+49 (0)345 5582–765
WWW:		http://www.mpi-halle.mpg.de/~theory

Persönliche Details

Geburtsdatum:	30. November 1968
Geburtsort:	Karatau, UdSSR
Geschlecht:	männlich
Staatsangehörigkeit:	Deutscher
Ehestand:	verheiratet mit Elena Ernst
Kinder:	Alice, Martha and Arina

Wissenschaftliche Ausbildung

1985–1991 Studium der Physik, Universität Tomsk, Russland

Schwerpunkte: Theoretische Physik, Festkörperphysik und Mathematik

1991 Diplom mit 'ausgezeichnet' in Physik

Lehrstuhl für Theoretische Physik, Universität Tomsk, Russland

Anleitung: Prof. Dr. Vladimir Kusnetzov

Diplomarbeit: *Indirekte Wechselwirkung der magnetischen Momenten*

1991–1993 Aspirantur, Universität Tomsk, Russland

Schwerpunkte: Theoretische Physik, Festkörperphysik und Mathematik

Unterbrechung wegen Umsiedlung nach Deutschland

1997 Promotion in Physik mit der Gesamtnote *magna cum laude*

Arbeitsgruppe "Theorie komplexer und korrelierter Elektronensysteme" der Max–Planck–Gesellschaft, TU Dresden

Anleitung: Prof. Dr. Helmut Eschrig

Doktorarbeit: *Full-potential-Verfahren mit einer kombinierten Basis für die elektronische Struktur*

Wissenschaftlicher Werdegang

1993–1996 Doktorand

Max-Planck-Arbeitsgruppe "Theorie komplexer und korrelierter Elektronensysteme"

Anleitung: Prof. Dr. Helmut Eschrig

1997-1999 Post-Doc

Daresbury Laboratory, Großbritannien

Anleitung: Prof. Dr. Walter Temmerman

Seit 1999 Wissenschaftler (befristet bis 15.08.2008)

Max-Planck-Institut für Mikrostruktur Physik, Halle (Saale)

Anleitung: Prof. Dr. Patrick Bruno (Abteilung Theorie)

Halle (Saale), den May 10, 2007

Dr. Arthur Ernst

P. Publications

P.1. List of the appended Publications

1 (s. P2ff) D. A. Rowlands, A. Ernst, B. L. Györffy, and J. B. Staunton *Density functional theory for disordered alloys with short-range order: Systematic inclusion of charge-correlation effects.* **Physical Review B 73**, 165122/1-18 (2006).

2 (s. P20ff) D. Ködderitzsch, H. Ebert, D. A. Rowlands and A. Ernst. *Relativistic formulation of the Korringa-Kohn-Rostoker non-local coherent-potential approximation.* **New Journal of Physics 9**, (81), 1-17 (2007).

3 (s. P37ff) A. Ernst, L. M. Sandratskii, M. Bouhassoune, J. Henk, M. Lüders. *Weakly dispersive band near the Fermi level of GaMnAs due to Mn interstitials.* **Physical Review Letters 95** (23), 237207/1-4 (2005).

4 (s. P41ff) S. Ostanin, A. Ernst, L. M. Sandratskii, P. Bruno, M. Däne, I. D. Hughes, J. B. Staunton, W. Hergert, I. Mertig, and J. Kudrnovský. *Mn-stabilised zirconia: from imitation diamonds to a new potential high T_C ferromagnetic spintronics material.* **Physical Review Letters**, **98**, 016101/1-4 (2007).

5 (s. P45ff) M. Lüders, A. Ernst, M. Däne, Z. Szotek, A. Svane, D. Ködderitzsch, W. Hergert, B. L. Györffy, and W. M. Temmerman. *Self-interaction correction in multiple scattering theory.* **Physical Review B 71** (20), 205109/1-17 (2005).

6 (s. P62ff) I. D. Hughes, M. Däne, A. Ernst, W. Hergert, M. Lüders, J. Poulter, J. B. Staunton, A. Svane, Z. Szotek, and W. M. Temmerman. *Lanthanide contraction and magnetism in the heavy rare earth elements.* **Nature 446**, 650-653 (2007).

7 (s. P67ff) C. Tusche, H. L. Meyerheim, N. Jedrecy, G. Renaud, A. Ernst, J. Henk, P. Bruno, and J. Kirschner. *Oxygen-induced symmetrization and structural coherency in Fe/MgO/Fe(001) magnetic tunnel junctions.* **Physical Review Letters 95** (17), 176101/1-4 (2005).

8 (s. P71ff) C. Tusche, H. L. Meyerheim, N. Jedrecy, G. Renaud, A. Ernst, J. Henk, P. Bruno, and J. Kirschner. *Reply to the Comment on "Destructive effect of disorder and bias voltage on interface resonance transmission in symmetric tunnel junctions".* **Physical Review Letters 96** (11), 119602/1 (2006).

9 (s. P72ff) W. Wulfhekel, A. Ernst, J. Henk, P. Bruno, J. Kirschner, F. Zavaliche, C. C. Kuo, M.-T. Lin. *Large spin effects in Coulomb blockade of Fe/MgO/Fe tunnel junctions.* **Physical Review B 72** (21), 212407/1-4 (2005).

10 (s. P76ff) R. Lindsay, A. Wander, A. Ernst, B. Montanari, G. Thornton, and N. M. Harrison. *Revisiting the surface structure of $TiO_2(110)$: A quantitative low-energy electron diffraction study.* **Physical Review Letters 94** (24), 246102/1-4 (2005).

11 (s. P80ff) C. R. Ast, J. Henk, A. Ernst, L. Moreschini, M. C. Falub, D. Pacilé, P. Bruno, K. Kern, and M. Grioni. *Giant spin splitting through surface alloying.* **Physical Review Letters**, **98**, 186807/1-4 (2007).

12 (s. P84ff) A. Ernst, J. Henk, M. Lüders, Z. Szotek and W. M. Temmerman. *Quantum-size effects in ultrathin Ag films on V(001): Electronic structure and photoelectron spectroscopy.* **Physical Review B 66**, 165435 (2002).